

A system with 128 OPMs can outperform a system with 275 SQUIDs

Konstantinos Tsilimparis¹, Robert Oostenveld¹

¹Donders Institute for Cognitive Neuroscience, Radboud University, Nijmegen, The Netherlands

Contents

1	Introduction	2
2	Methods	9
2.1	Comparing the sensor arrays	9
2.1.1	Description of the SQUID MEG system	9
2.1.2	Description of the OPM MEG system	9
2.1.3	Number of sensors and spatial resolution	10
2.2	Somatosensory experiment	12
2.2.1	Data acquisition	12
2.2.2	Co-registration	13
2.2.3	Processing of experimental data	13
2.3	Simulation of somatosensory activity	14
2.4	Whole brain simulations	15
2.5	Quantifying source reconstruction accuracy	16
2.5.1	Dipole moment uncertainty	17
2.5.2	Dipole position uncertainty	19
3	Results	20
4	Discussion	33
5	Conclusion	37
6	Data and code availability	38
7	Supplementary material	38
8	References	44

1 Introduction

Researchers and clinicians use magnetoencephalography (MEG) to measure the magnetic fields generated by brain activity, localize neural activity and differences in activity. MEG systems are comprised of sensors that are placed outside of the head and that typically cover the whole head. These sensors have to be extremely sensitive in order to pick up brain activity, which is approximately 10 billion times weaker than the earth's magnetic field ([Baillet et al., 2001](#)). To suppress the earth's magnetic field and other types of environmental noise that interfere with the recording of the brain signals, MEG systems are placed in a magnetic shielded room (MSR) ([Baillet et al., 2001](#); [Singh, 2014](#)). MEG can capture changes in brain activity with millisecond precision ([Fred et al., 2022](#)) and it allows to reconstruct the location of brain activity with ~2-3 mm accuracy ([Singh, 2014](#), [Fred et al., 2022](#)). With these characteristics, MEG has higher temporal resolution compared to functional magnetic resonance imaging (fMRI) and higher spatial resolution compared to electroencephalography (EEG). Consequently, MEG is a valuable tool for neuroscientific research and clinical applications.

For a long time the only magnetic field sensors sensitive enough to pick up the brain activity were based on superconducting quantum interference devices (SQUIDs). SQUIDs require cryogenic cooling close to absolute zero (-273°C). For the cooling to occur, the SQUID sensors are bathed in liquid helium and placed into a fixed array in a so-called dewar that fits around the participant's head ([Singh, 2014](#)).

The main disadvantage of SQUIDs is their dependence on cryogenic cooling. Cryogenic cooling relies on liquid helium that constantly evaporates (i.e., boils off) and hence needs to be refilled. Liquid helium has high costs, making the operational costs of a SQUID-based MEG system expensive. Additionally, the cryogenic cooling requires insulation

between the sensors and the scalp, both to protect the skin surface against the cold and to prevent the helium from evaporating too fast. As a result, the sensors are placed at minimum 1.5-2 cm away from the scalp in a fixed array that cannot adapt to different head sizes or shapes ([Hill et al, 2020](#)). The large helium-filled dewar containing the SQUID array cannot move along with the participant and hence requires the subject's head to be fixed during the experiment. Any movement of the head relative to the fixed sensor array blurs the field topography, increases the error in localizing brain sources and decreases the statistical sensitivity ([Stolk et al, 2013](#)). For these reasons, the neuroscientific community has turned its focus toward a new MEG system which does not require cryogenic cooling but that is based on optically pumped magnetometers (OPMs).

OPMs are the sensors used in the new generation MEG systems. Studies have demonstrated their ability to sense fields as small as those produced by the human brain ([Boto et al., 2017](#); [Boto et al., 2018](#)). OPM sensors are based on an alkali metal in a gaseous state (usually rubidium) that is contained in a vapor cell, integrated with a laser and a photo detector. They are individual sensors ([Fig. 1A](#)) that allow the researcher freedom to choose where to place them over the head ([Brookes et al., 2022](#)). This is especially crucial when working with a limited number of sensors, as that allows to strategically target brain regions of interest. In this master's thesis, however, we do not study the advantages of this strategic placement but rather consider systems with whole-head coverage.

The main advantage of OPMs is that they don't need cryogenic cooling and liquid helium, reducing the maintenance costs and environmental impact. In comparison to cryogenic SQUID sensors, an OPM sensor requires significantly less insulation between its vapor cell (which is heated to provide enough rubidium vapor) and the scalp. Consequently, the vapor cell can be placed a few millimetres away from the scalp ([Brookes et al, 2022](#)) and the sensor can be held in place in flexible caps or adjustable 3D-printed helmets suitable for

any head size ([Fig. 1B](#)). Since the MEG signal strength decreases with the square of distance from the source (inverse square law), the closer a sensor is to the brain, the higher the MEG signal strength it picks up ([Brookes et al, 2022](#)). Therefore, OPMs detect brain signals with a higher amplitude compared to SQUIDs, especially from superficial cortical areas. Another advantage of OPMs is that the sensors can move together with the participant, allowing for participant's head movements during the experiment ([Seymour et al, 2021](#)). This opens up possibilities to study brain activity in more realistic settings that require or involve movement such as gait experiments, typically studied using EEG ([Stokkermans et al., 2023](#)) or functional near-infrared spectroscopy ([Cockx et al., 2024](#)). Additionally, it allows researchers to study the brain activity of individuals who have difficulty sitting still, such as children ([Corvilain et al., 2023](#)) and epilepsy patients during seizures ([Hillebrand et al., 2023](#)). Given these advantages, OPMs have transitioned from physics research institutes to commercial development and are now being adopted by clinics and neuroscience research institutes, including the Donders Institute.

At the Donders Institute we acquired a FieldLine OPM system comprised of 32 sensors and an adult-sized “smart” helmet with a total of 144 slots. Individual sensors can be placed freely in any of the slots. Each slot allows the sensor to move along a single axial direction. That way, the sensor can slide in its slot towards the head surface until it touches, regardless of the head size and shape. At the start of each MEG session the system automatically localizes the position of each sensor in the helmet ([Alem et al., 2023](#)). We installed our OPM system in the same MSR as our current 275-sensor CTF SQUID system. Although OPMs allow movement, we will not consider this in the research presented here. In the MSR the background magnetic field (e.g., due to earth's magnetic field) is attenuated but not fully suppressed. When sensors move or rotate due to head movements, they pick up the changes in this background magnetic field, resulting in artifacts that degrade the MEG signal. Because of the movement, the magnetic field changes might exceed the sensors'

dynamic range (i.e., the range of magnetic fields they are able to detect) resulting in saturation of the signal ([Brookes et al., 2022](#)). To mitigate these issues, we stabilise the helmet by mounting it on a wooden plate ([Fig. 1B](#)). So, in this master's thesis we compare OPMs to SQUIDs by flexibly positioning OPMs closer to the scalp, but still assuming head-fixed experiments.

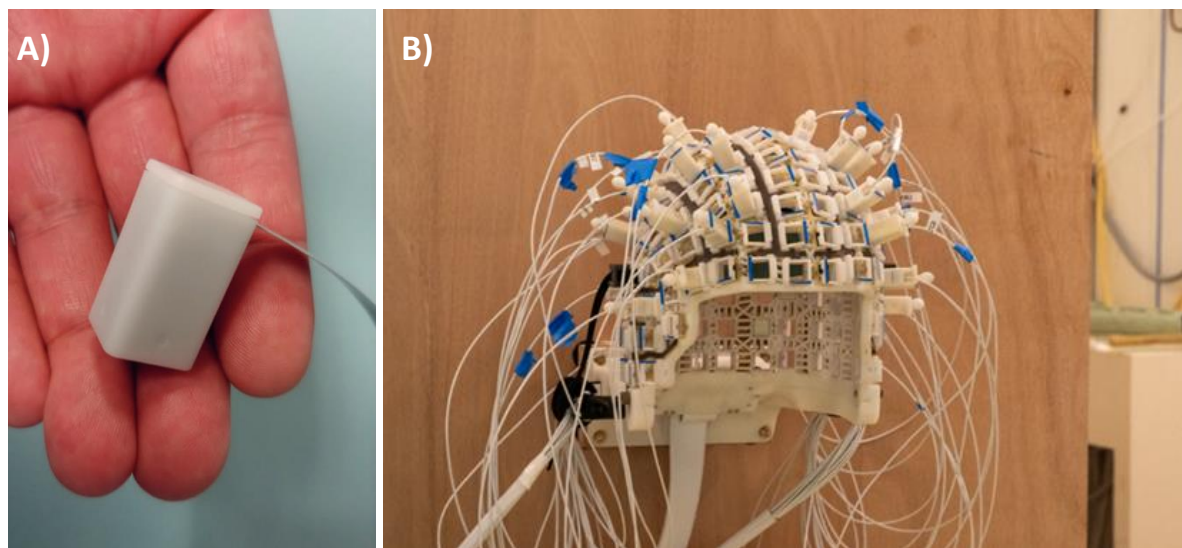


Fig. 1. OPM sensors and helmet at the Donders Institute. A) Single FieldLine v3 OPM sensor.

From [Alem et al. \(2023\)](#). Copyright 2023 by Alem, Hughes, Buard, Cheung, Maydew, Griesshammer, Holloway, Park, Lechuga, Coolidge, Gerginov, Quigg, Seames, Kronberg, Teale and Knappe. **B)** The OPM sensors placed in the helmet, which is mounted on a wooden plate. The helmet has 144 slots that allow the sensors to slide in until they touch the subject's scalp.

Positioning OPMs closer to the scalp leads to larger signals from brain sources, improved signal-to-noise ratio (SNR) and thereby higher source reconstruction accuracy ([Hill et al., 2024](#)). However, it should be noted that not only the brain signals picked up by the

OPMs are larger, but OPM sensors also have a higher intrinsic noise (7-10 fT/sqrt(Hz) compared to 2-5 fT/sqrt(Hz) for SQUIDS; [Brookes et al., 2022](#)). Thus, the improved SNR due to closer proximity of the sensor to the scalp primarily applies to superficial cortical activity, whereas for deeper sources the advantage of closer proximity is outweighed by the higher intrinsic sensor noise ([Brookes et al., 2022](#)). The SNR can be used to quantify the neural activity's strength relative to the sensor and background noise for individual sensors. However, as we use an array with a large number of sensors to measure the spatial topography, the MEG system performance should not be considered per sensor but for the array as a whole. Source reconstruction accuracy quantifies how accurately we can estimate the strength and position of the neural activity within the brain based on the signal measured by all MEG sensors. [Boto and colleagues \(2016\)](#) conducted simulations demonstrating that an OPM system, with equal sensor number and noise to a SQUID system, has a fivefold improvement in SNR and has improved accuracy of beamformer source reconstruction. In a separate study, [Ivanainen and colleagues \(2017\)](#) performed simulations comparing OPMs and SQUIDS with equal sensor numbers, but now assuming the OPMs to have sensor noise two times higher than the SQUIDS. In this case the OPMs showed a 2.7-fold improvement in SNR, while they exhibited similar localisation accuracy across the entire brain and better localization accuracy for superficial sources. These studies highlighted the improved SNR and source reconstruction accuracy of OPMs over SQUIDS, but also reveal that the sensor noise of the OPMs plays a role. Furthermore, they do not study the effect of the number of OPM sensors on the comparison. The noise per sensor and the number of sensors both affect the source reconstruction accuracy; as the noise level of individual OPMs differs from that of individual SQUIDS, comparisons between SQUID and OPM sensors should take both the sensor number and sensor noise into account. In general, the higher noise of the individual OPM sensors can be compensated partially by the closer placement to the brain and partially by increasing the number of OPM sensors. Since OPMs can be purchased and

placed as individual sensors, we should choose how many sensors to get. For example, at the Donders Institute, we currently have 32 OPM sensors and plan to get more in the future. This raises the question: how many OPM sensors should we get?

This study aims to provide an answer to this question by investigating how source reconstruction accuracy depends on the number of OPM sensors. We quantify source reconstruction accuracy using two metrics: the dipole moment uncertainty (DMU) and the dipole position uncertainty (DPU). DMU quantifies how accurately we estimate the strength of the neural activity (the dipole moment), while DPU quantifies how accurately we estimate the position of a dipole that represents the neural activity. DMU is important for cognitive scientists since they often design experiments that manipulate the strength of the neural activity in different experimental conditions. An example is the N400 experiment ([Fig. 2; Cruse et al, 2014](#)) that relates to the semantic processing. In Figure 2, DMU is proportional to the standard error (shaded areas). The lower the standard error (i.e., the lower the DMU), the better we can differentiate the two conditions. This means that a MEG system with low DMU allows cognitive scientists to use less trials and/or add more conditions, while still being able to differentiate the conditions. In contrast, DPU is particularly important when considering single conditions, for example for a clinician localizing the focus of epileptiform activity in a patient. Low DPU allows clinicians to identify this location with greater accuracy, contributing to subsequent surgical planning for resecting the source of epileptic seizures. In conclusion, DMU and DPU provide related but non-identical insights into how the source reconstruction accuracy of OPMs depends on the number of sensors.

We specifically tackle the research question how many sensors are required for an OPM system to perform equally well as the 275-sensor CTF SQUID system, which is our reference system. In simulations and measurements, we vary the number of OPM sensors which we place uniformly over the surface of the head. We perform an experiment with left

median nerve stimulation on a single participant using both the SQUID and the OPM system. This is a well-studied and replicated experiment ([Andersen & Dalal, 2021](#); [Boto et al., 2017](#); [Buchner et al., 1994](#)), the activity of which can be modelled 20 ms post-stimulation with a dipole located at the right Primary Somatosensory (S1) area. To validate the results from the experiment, we also simulate a dipole at the right S1 area. In both the simulations and the experiment, we compare the DMU and DPU between the SQUID and OPM system. Subsequently, we simulate dipoles on the whole cortical surface to see how the effect of the number of OPM sensors on the DMU and DPU generalizes towards the rest of the brain.

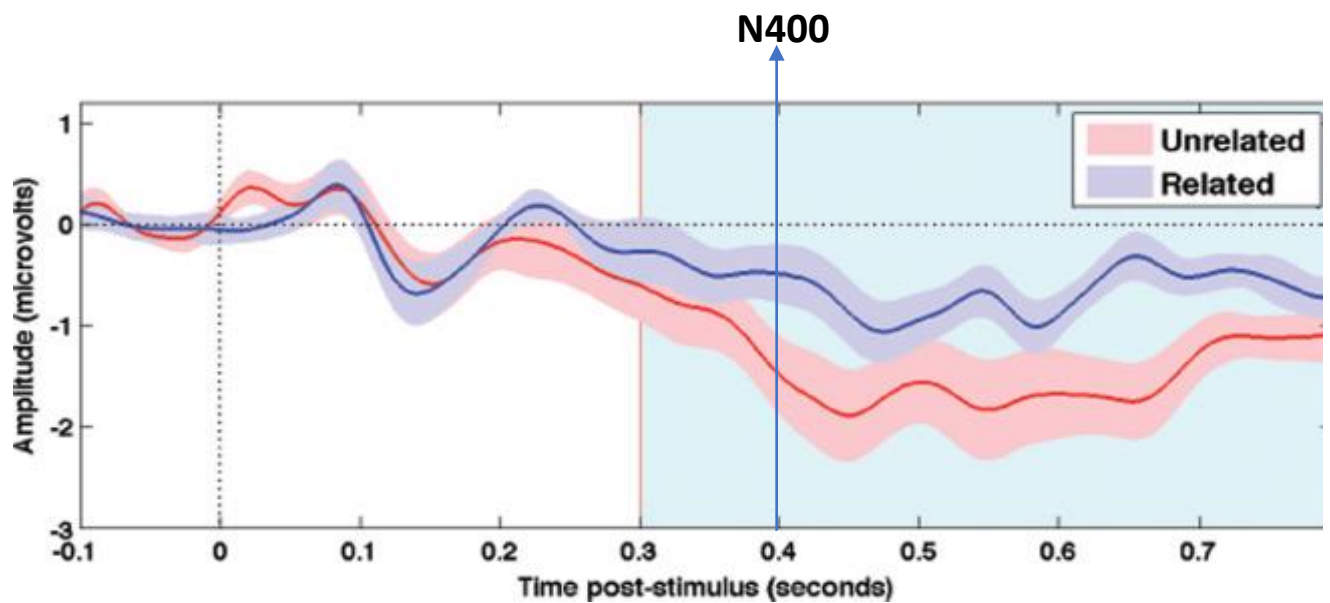


Fig. 2. The N400 experiment. Event-related potentials for two conditions are illustrated: the unrelated condition (red) where words are incongruent with the context of the sentence (e.g., 'I take my coffee with cream and mud') and the related condition (blue) where words are congruent with the context of the sentence (e.g., 'I take my coffee with cream and sugar'). Dipole moment uncertainty (DMU) is proportional to the standard error (shaded areas). The lower the standard error (i.e., the lower the DMU), the better we can

differentiate the two conditions. This mean that a MEG system with low DMU increases statistical sensitivity to detect a condition difference around 400 ms, which subsequently translates in the option of using less trials and/or add more conditions in the experimental design. From [Cruse et al. \(2014\)](#). Copyright 2014 Cruse, Beukema, Chennu, Malins, Owen, McRae.

2 Methods

2.1 Comparing the sensor arrays

2.1.1 Description of the SQUID MEG system

The CTF SQUID system (CTF MEG Neuro Innovations Inc, Coquitlam, BC, Canada) consists of 275 axial gradiometers. At the time of the experiment, two SQUID sensors were non-functional. Therefore, we used the rest 273 axial gradiometers and kept their position fixed. During the experiment we had the participant seated comfortably in the helmet according to normal lab procedures and used head localizer coils to co-register the SQUID sensor positions with the head model that was made on basis of the individual's anatomical MRI. In the whole-brain simulations we used all 275 axial gradiometers. Consequently, we generated a head model from an average brain and placed the 275 SQUID sensors symmetrically around the head.

2.1.2 Description of the OPM MEG system

The FieldLine OPM system (Boulder, Colorado) consists of a helmet that can accommodate up to 144 OPM sensors measuring the magnetic field in the radial direction. We used 32 OPM sensors in the experiment and performed 6 runs in which we varied the placement of the sensors over the helmet to achieve coverage over all the slots. We kept 9 sensors at the same position over all runs to fixate the head and to prevent head movement between runs. The remaining 23 sensors were placed differently over the 6 runs. In the analysis we computed an average event-related field (ERF) per run and concatenated these ERFs over all runs to effectively obtain an ERF with 144 sensors from which we could subsequently take subsamples with fewer sensors.

In both the experiment and simulations, we varied the number of OPM sensors from 16 to 128 in steps of 16, resulting in eight different sensor configurations. For each sensor count, we ensured that the selected subset of sensors was uniformly distributed and identical in the experiment and the simulations.

2.1.3 Number of sensors and spatial resolution

Our goal was to determine the number of OPM sensors to achieve similar dipole moment uncertainty (DMU) and dipole position uncertainty (DPU) as with the 275-sensor SQUID system. However, the relationship between DMU, DPU, and the number of OPM sensors is not straightforward. By placing additional sensors at unique locations in between existing sensors, not only does the number of sensors increase, but also the sensor coverage and the spatial resolution of the OPM system ([Fig. 3A](#)). The spatial resolution of the OPM system is defined as the number of unique sensor locations divided by the sensor coverage and it increases when we place the sensors closer to each other.

It is expected that source reconstruction accuracy depends not only on the number of sensors, but also on the sensor coverage and spatial resolution, especially for those sensors that are placed directly above the source of interest. In simulations we can separate these parameters (number of sensors, versus sensor coverage and spatial resolution) in a way that is not possible in real recordings. By placing new sets of sensors virtually on top of the existing ones, we can increase the number while keeping the sensor coverage and spatial resolution constant ([Fig. 3B](#)).

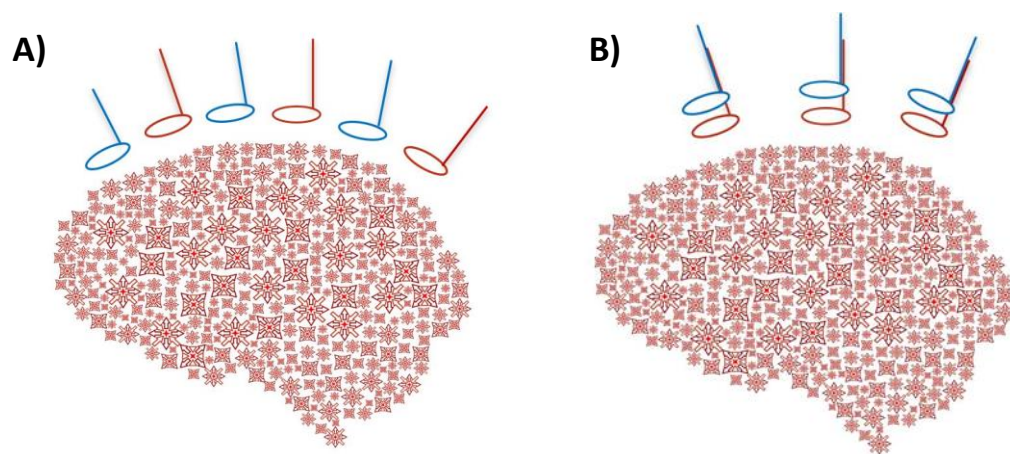


Fig. 3. Spatial resolution of the OPM system. In our simulations we manipulate the number of sensors, by which also the spatial resolution of the OPM system can change. We explicitly consider two options. A) We increase the spatial resolution by placing the additional blue sensors in between the red sensors; this is a more realistic scenario. B) We keep the spatial resolution the same by placing the additional blue sensors virtually on top of the red sensors; this is a purely theoretical scenario. In both cases the recording locations are distributed homogeneously around the head, but coverage might be slightly different.

2.2 Somatosensory experiment

2.2.1 Data acquisition

A single participant took part in the experiment. The participant gave written, informed consent prior to the experiment in line with the ethics approval. A left median-nerve stimulation experiment was carried out. During the experiment, we administered electrical shocks to the left median nerve with a jittered inter-stimulus interval between 800 and 1200 ms. We expected the brain response 20 ms post stimulation to localize with a dipole at the right S1 area ([Buchner et al., 1994](#)). The participant performed the same task using both the 32-sensor OPM and the 275-sensor SQUID systems. The data from the OPM system was sampled at 5000 Hz and that from the SQUID system was sampled at 1200 Hz.

The OPM system was placed in the same MSR as the SQUID system. Without additional noise cancellation (i.e., nulling coils that can perform static and dynamic noise cancellation), the background magnetic field was ~ 50 nT at the center of the MSR. Even with this background field, our sensors stayed within their dynamic range. So, we performed the experiment without the nulling coils.

Our OPM system is limited to 32 sensors, which can be placed in 144 helmet slots. To acquire a measurement for each slot, we divided the experiment into six runs while maintaining the participant's head in a fixed position. We kept 9 sensors around the participant's head fixed for each run. Since the OPM sensors touched the participant's head, these 9 sensors were able to keep the participant's head fixed throughout the experiment. In between runs we moved the remaining 23 sensors to fill every helmet slot. In our data analysis we combined the six experimental runs to represent a single experiment with 144 sensors.

2.2.2 Co-registration

For the SQUIDs we co-registered the anatomical MRI to the SQUID array based on three head localizer coils placed at anatomical landmarks (the nasion, the left and right ear canal) and the Polhemus head shape. For the OPMs we co-registered the anatomical MRI to the OPM helmet using a 3D scan of the participant's face and helmet ([Zetter et al., 2019](#)). The procedure consists of two steps: we first co-registered the 3D scan of the face with the face reconstructed from the anatomical MRI, subsequently we co-registered the 3D scan of the frontal rim of the helmet with a reference helmet. Since the 3D scan represents both the face and the rim of the helmet, this allows to align the anatomical MRI with the reference helmet. In retrospect, the co-registration using a 3D scan was not totally accurate, resulting in systematically shifted dipoles in the OPM measurements relative to the SQUID measurements. Specifically, the distance between the dipoles in the OPM and the SQUID measurement was approximately 10 mm (see [Supplementary Material Fig. A4](#)). However, this shift has no consequence for the DMU and DMU estimates, as these estimates are relative to the optimally fitted dipole positions.

For the SQUIDs, two sensors did not work during the experiment, resulting in a final count of 273 SQUID sensors. For the OPMs, we excluded duplicate sensors between the 6 experimental runs and sensors that appeared inside the subjects' heads after the co-registration, resulting in a final count of 135 OPM sensors. We varied the number of the OPM sensors as reported in [Section 2.1.3](#).

2.2.3 Processing of experimental data

We analyzed the data with the FieldTrip toolbox ([Oostenveld et al., 2011](#)). For the SQUIDs, we segmented the continuously recorded data in 600 ms trials time-locked to the left median nerve stimulation, with a 200 ms prestimulus baseline period. We applied

baseline correction and rejected trials that had high variance, resulting in 146 trials.

Subsequently, we averaged all trials to compute an ERF with 273 sensors.

The preprocessing steps for the OPMs were identical to those for the SQUIDs. The OPM experiment consisted of six runs, each with 146 trials. In addition to the SQUIDs preprocessing steps, for the OPMs we excluded one sensor with high variance from one run, resulting in 134 sensors. For each run we also applied an extra denoising technique called homogeneous field correction (HFC) ([Tierney et al., 2021](#)). HFC is a method for denoising MEG data based on a spatially homogeneous model of the background magnetic field across the OPM array. This method has previously been used successfully for reducing magnetic interference in OPM magnetometers (see [Supplementary Material Fig. A3](#); [Hill et al., 2022](#); [Mellor et al., 2023](#); [Seymour et al., 2022](#)) that are more sensitive to the environmental noise than the SQUID gradiometers. Subsequently, we averaged all trials per run to compute an ERF per run. We concatenated these ERFs over all runs to effectively obtain an ERF with 134 sensors.

2.3 Simulation of somatosensory activity

First, we kept the spatial resolution of the OPM system the same by virtually placing each new set of sensors on top of the existing sensors. Subsequently, we increased the spatial resolution of the OPM system along with the sensor number by placing additional sensors at different locations.

For both SQUIDs and OPMs, we simulated data using a forward model of a single dipole placed in the right S1 area (as determined from the experimental data). As in the experimental data, we simulated 146 trials, each with a duration of 600 ms and a sampling frequency of 1200 Hz. We added Gaussian noise to the sensors that was independent over

sensors and of equal magnitude on all sensors. The magnitude of the sensor noise of the SQUIDs was estimated to be 5 fT based on empty room recordings of our CTF SQUID system (4 - 8 fT/VHz). The sensor noise of the OPMs was set to be three times higher than that of the SQUIDs based on the noise level (20 ± 5 fT/VHz) of the FieldLine OPM system as reported in literature ([Alem et al., 2023](#)). Subsequently, we averaged all trials to compute an ERF with 273 sensors for the SQUIDs and an ERF with 134 sensors for the OPMs.

2.4 Whole brain simulations

For the SQUID system simulations, we manually determined the position of the head within the SQUID helmet. First, we made sure the SQUID array covered the cortex uniformly and symmetrically along the left–right axis. Secondly, we verified that the sensor positions were at least 2 cm away from the scalp, which approximates the thickness of the SQUID system dewar ([Iivanainen et al., 2017](#)). For the OPM system simulations, we projected the sensors onto the scalp and we varied the number of sensors as reported in [Section 2.1.3](#).

For both SQUID and OPM, we simulated sources on the cortical surface, which was extracted from the anatomical MRI of an average of 27 T1 scans of the same subject ([Holmes et al., 1998](#)) using Freesurfer (<http://surfer.nmr.mgh.harvard.edu>). To calculate DMU, we simulated data from 20,484 individual sources at the vertices of the triangular cortical mesh and to calculate DPU we simulated data from 5124 sources. We modelled less sources for the DPU than the DMU, since DPU calculation is computationally heavier. Each source was oriented perpendicular to the cortical surface. We added Gaussian sensor noise that was independent over sensors and of equal magnitude on all sensors. As in the simulation of a dipole at the right S1 area, we specified the sensor noise of the OPMs to be three times higher than that of the SQUIDs.

2.5 Quantifying source reconstruction accuracy

Source reconstruction is based on forward and inverse modelling techniques.

Forward modelling describes how the neural sources generate magnetic fields detectable by the MEG sensors outside the head ([Mosher et al., 1999](#)). It essentially models how the electric currents flow through different head tissues, such as the white and grey matter, cerebrospinal fluid, skull bone and skin. In our data, to compute the forward model, we constructed a single sphere MEG volume conduction model for both OPMs and SQUIDs representing the interface between the brain and the skull ([Mosher et al., 1999](#); [Ilmoniemi et al., 1985](#)). Inverse modelling estimates the source parameters (dipole moment and position) based on these detected magnetic fields ([Mosher et al., 1999](#)). The inverse problem is ill-posed. To solve it, we make certain assumptions about the sources (e.g., that there is only one or a few dipolar sources). There is a linear relationship between the dipole moment and the forward model. On the contrary, the relation between the dipole position and the forward model is non-linear. In this master's thesis, we perform source reconstruction through dipole fitting, assuming a single dipolar source. The position of this source is iteratively optimized through a gradient descent method.

We can use three methods to compute DMU and DPU: i) analytic solution (see [section 2.5.1](#)), ii) jackknife resampling ([Quenouille, 1956](#)), and iii) Monte Carlo simulations ([Metropolis & Ulam, 1949](#)). Results from these three methods are directly comparable and can be used interchangeably (see [Supplementary Material Fig. A2](#)). Since the relationship between the dipole moment and the forward model is linear, we derive and use an analytic solution for DMU. However, the relationship between the dipole position and the forward model is non-linear, making an analytic solution for DPU more complex to find. Therefore, we use the jackknife resampling and Monte Carlo simulations for DPU.

2.5.1 Dipole moment uncertainty

The MEG forward model states that the magnetic fields \mathbf{y} , produced by a single dipolar source with dipole strength q , and measured by M MEG channels are given by,

$$\mathbf{y} = \mathbf{L}_\alpha(\mathbf{r})q + \mathbf{e} \quad (1)$$

Here, $\mathbf{L}_\alpha(\mathbf{r})$ is the $M \times 1$ forward field for a source with position \mathbf{r} and orientation α . \mathbf{e} represents the noise that can originate from the sensors and the environment.

We aim to calculate the dipole moment uncertainty (DMU). For this reason, we acquire K individual measurements (e.g., by repeating the experiment K times), each represented by Equation 1. We stack these K measurements into a $M \times K$ matrix \mathbf{Y} ,

$$\mathbf{Y} = \mathbf{L}_\alpha(\mathbf{r})\mathbf{Q} + \mathbf{E} \quad (2)$$

where \mathbf{Q} is $1 \times K$ and \mathbf{E} is $M \times K$.

To estimate the dipole moment $\hat{\mathbf{Q}}$, we invert Equation 2

$$\hat{\mathbf{Q}} = \mathbf{L}_\alpha^+(\mathbf{r})\mathbf{Y} = \mathbf{L}_\alpha^+(\mathbf{r})(\mathbf{L}_\alpha(\mathbf{r})\mathbf{Q} + \mathbf{E}) = \mathbf{Q} + \mathbf{L}_\alpha^+(\mathbf{r})\mathbf{E} \quad (3)$$

where $\mathbf{L}_\alpha^+(\mathbf{r})$ denotes the pseudo-inverse of $\mathbf{L}_\alpha(\mathbf{r})$.

This gives us

$$\hat{\mathbf{Q}} - \mathbf{Q} = \mathbf{L}_\alpha^+(\mathbf{r})\mathbf{E} \quad (4)$$

The *DMU*, which mathematically is the standard deviation of the estimated dipole moment over the K individual measurements, is

$$DMU \equiv \text{Std}(\hat{q}) \equiv \sqrt{\frac{\sum_{i=1}^K (\hat{q}_i - q_i)^2}{K}} = \sqrt{\frac{(\hat{\mathbf{Q}} - \mathbf{Q})(\hat{\mathbf{Q}} - \mathbf{Q})^T}{K}} \quad (5)$$

Combining Equations 4 and 5,

$$DMU = \sqrt{\frac{\mathbf{L}_\alpha^+(\mathbf{r}) \mathbf{E} \mathbf{E}^T (\mathbf{L}_\alpha^+(\mathbf{r}))^T}{K}} = \sqrt{\mathbf{L}_\alpha^+(\mathbf{r}) \mathbf{\Sigma}_N (\mathbf{L}_\alpha^+(\mathbf{r}))^T} \quad (6)$$

where $\mathbf{\Sigma}_N \equiv \frac{1}{K} \mathbf{E} \mathbf{E}^T$ is the noise covariance matrix.

In our simulations, we assume that there is only sensor noise which is independent over channels and of equal magnitude on all channels. As a result, the covariance matrix $\mathbf{\Sigma}_N$ has non-zero values only on its diagonal. Each diagonal element represents the variance of the sensor noise, σ_N^2 . Hence, the noise covariance matrix becomes a scaled identity matrix:

$$\mathbf{\Sigma}_N = \sigma_N^2 \mathbf{I},$$

$$DMU = \sqrt{\sigma_N^2 \mathbf{L}_\alpha^+(\mathbf{r}) (\mathbf{L}_\alpha^+(\mathbf{r}))^T} = \sqrt{\sigma_N^2 \|\mathbf{L}_\alpha^+(\mathbf{r})\|^2} = \sqrt{\frac{\sigma_N^2}{\|\mathbf{L}_\alpha(\mathbf{r})\|^2}} \quad (7)$$

where $\|\mathbf{L}_\alpha(\mathbf{r})\| = \sqrt{\sum_{j=1}^M L_j^2}$ is the Frobenius-norm of the forward field $\mathbf{L}_\alpha(\mathbf{r})$.

DMU simplifies to the convenient formula

$$DMU = \frac{\sigma_N}{\|\mathbf{L}_\alpha(\mathbf{r})\|} \quad (8)$$

This formula is also used by [Brookes et al. \(2021\)](#) and [Hill et al. \(2024\)](#) within the beamformer framework. In contrast, we derive it more generally in relation to linear

estimation, which is used in minimum norm estimates and in estimating the source strength in dipole fitting.

To calculate DMU, for our experimental data we use Equation 5 since noise can originate from the sensors and the environment. In contrast, for our simulations we use Equation 8 since we assume that noise originates only from the sensors.

2.5.2 Dipole position uncertainty

We define the dipole position uncertainty (DPU) for a single dipolar source as the root mean square

$$DPU = \sqrt{\frac{\sigma_x^2 + \sigma_y^2 + \sigma_z^2}{3}} \quad (9)$$

where σ_i is the standard deviation of the estimated dipole positions in the direction i ([Vrba and Robinson, 2002](#)).

For our experimental data and simulation of a dipole at the right S1 area, we used the jackknife resampling. In this approach, we systematically left out one trial from the dataset and computed an ERF. Since we had 146 trials, we computed 146 ERFs in total and fitted a dipole to each one. Finally, we calculated the standard deviation of the estimated dipole positions along each of the three coordinate axes (σ_x , σ_y , σ_z) and corrected for the jackknife bias.

For our whole brain simulations, we used Monte Carlo simulations. For each source, we simulated 100 forward models contaminated with Gaussian noise and fitted a dipole to each forward model, resulting in 100 fitted dipole positions. Finally, we calculated the standard deviation of the estimated dipole positions along each of the three coordinate axes (σ_x , σ_y , σ_z).

3 Results

The somatosensory experiment does not allow us to control the noise, which can be both sensor and environmental noise, and separate the sensor number from the spatial resolution (see [section 2.1.3](#)). On the other hand, the simulation of the somatosensory activity allows us to control the level of the sensor noise and separate the sensor number from the spatial resolution (see [section 2.1.3](#)). Consequently, we first show results for the simulation of the somatosensory activity, which also allow to introduce the visual representation of the results.

[Figure 4](#) shows the dipole moment uncertainty (DMU) and dipole position uncertainty (DPU) for the simulated data with a dipole at the right S1 area. The simulated sensor noise for the OPMs is set to be three times higher than the SQUIDs and the spatial resolution of the OPM system remains the same, irrespective of the number of sensors (see [section 2.1.3](#)).

[Figure 4a](#) shows the DMU and DPU ratio for the two MEG systems plotted as a function of the number of OPM sensors. The DMU and DPU decrease with the number of sensors and hence OPM source reconstruction accuracy improves. However, the improvement in source reconstruction accuracy becomes smaller as the number of sensors increase.

Mathematically, both DMU and DPU decrease with the square root of the number of sensors. This is evident from the exponents: -0.5 for DMU (computed with the analytic solution) and -0.46 for DPU (estimated with the jackknife resampling). In [Figure 4b](#), we plot the DMU and DPU ratio (vertical axis) versus the number of sensors (horizontal axis) using logarithmic scales. The relationship becomes linear, with a slope of -0.5 for DMU and -0.46 for DPU, and an intercept that scales with the noise of the OPMs.

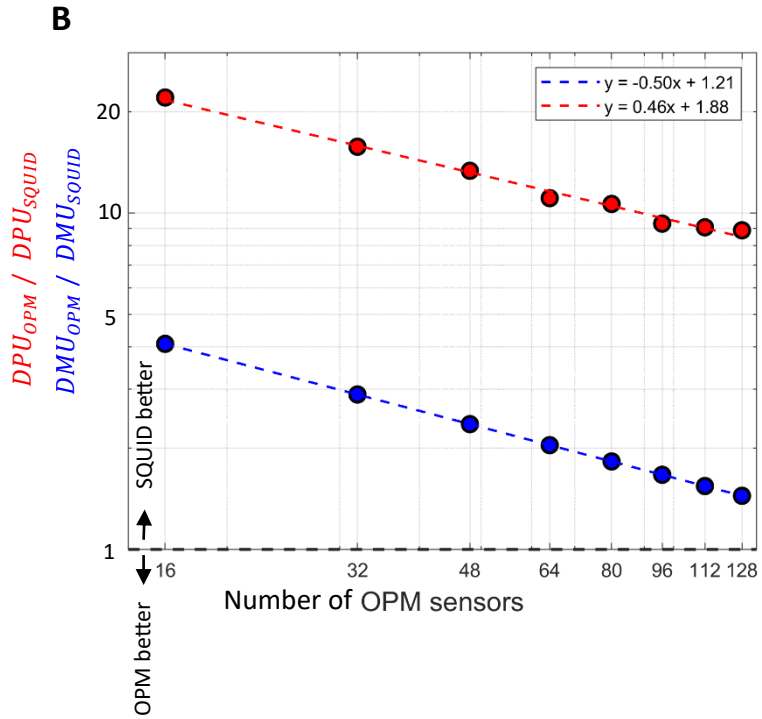
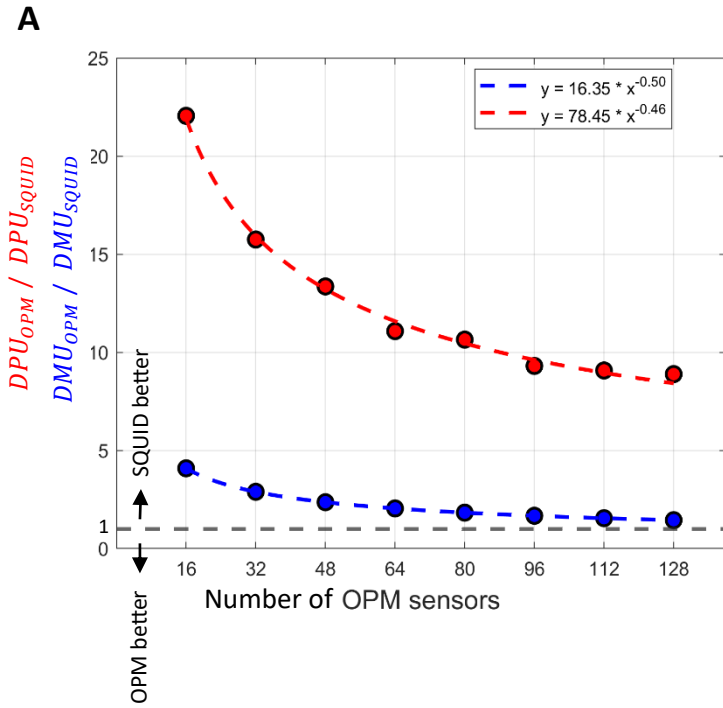


Fig. 4. Simulated data with constant spatial resolution. (A) The ratio of the dipole moment uncertainty (DMU; blue) and dipole position uncertainty (DPU; red) for the OPMs over the SQUIDs, plotted as a function of the number of OPM sensors. A polynomial is fitted to each set of points. When the DMU and DPU ratio equals 1 (horizontal black dashed line) OPMs and SQUIDs perform equally well. Below the horizontal black dashed line, the OPMs perform better and conversely, above the dashed line, SQUIDs perform better. (B) Same plot as in (A), but with the data along both axes displayed on a logarithmic scale. The intercept of the line fitted to the points scales with the noise of the OPMs relative to the noise of the SQUIDs.

As explained in [section 2.1.3](#), when we increase the number of sensors in a realistic system, the sensor coverage and spatial resolution also change. [Figure 4](#) shows results with constant spatial resolution, i.e., by placing sensors virtually on top of each other. In [Figure 5](#) we modelled the realistic scenario with an increase in the spatial resolution of the OPM system along with the number of sensors. Compared to the constant spatial resolution, the improvement of both DMU and DPU is more rapid as the number of OPM sensors increase. Both DMU and DPU benefit from the increased spatial resolution as well as the increased number of sensors. Mathematically, we demonstrated that DMU is inversely proportional to the Frobenius norm of the forward field, $||L||$ ([section 2.5.1](#), Eq. (8)). Considering the same number of sensors, but with an increasing spatial resolution (i.e., [Fig 3A versus B](#)) results in some sensors being closer to the peaks and consequently to a larger norm of the forward field (see [Supplementary Material Fig. A1](#)). The improvement in DPU can be explained by placing the sensors closer to each other which results in capturing better the gradients in the topography (i.e., the areas around the peaks of the dipolar pattern) (see [Supplementary Material Fig. A1](#)). The improvement of DPU is more rapid than the DMU, meaning that DPU benefits more from an increasing spatial resolution. Based on the ratio of the DMU for the OPMs over the SQUIDs, we conclude that a system with 128 OPMs performs equally well as a system with 273 SQUIDs. Based on the ratio of the DPU for the OPMs over the SQUIDs the performance of the systems becomes comparable at 112 OPMs.

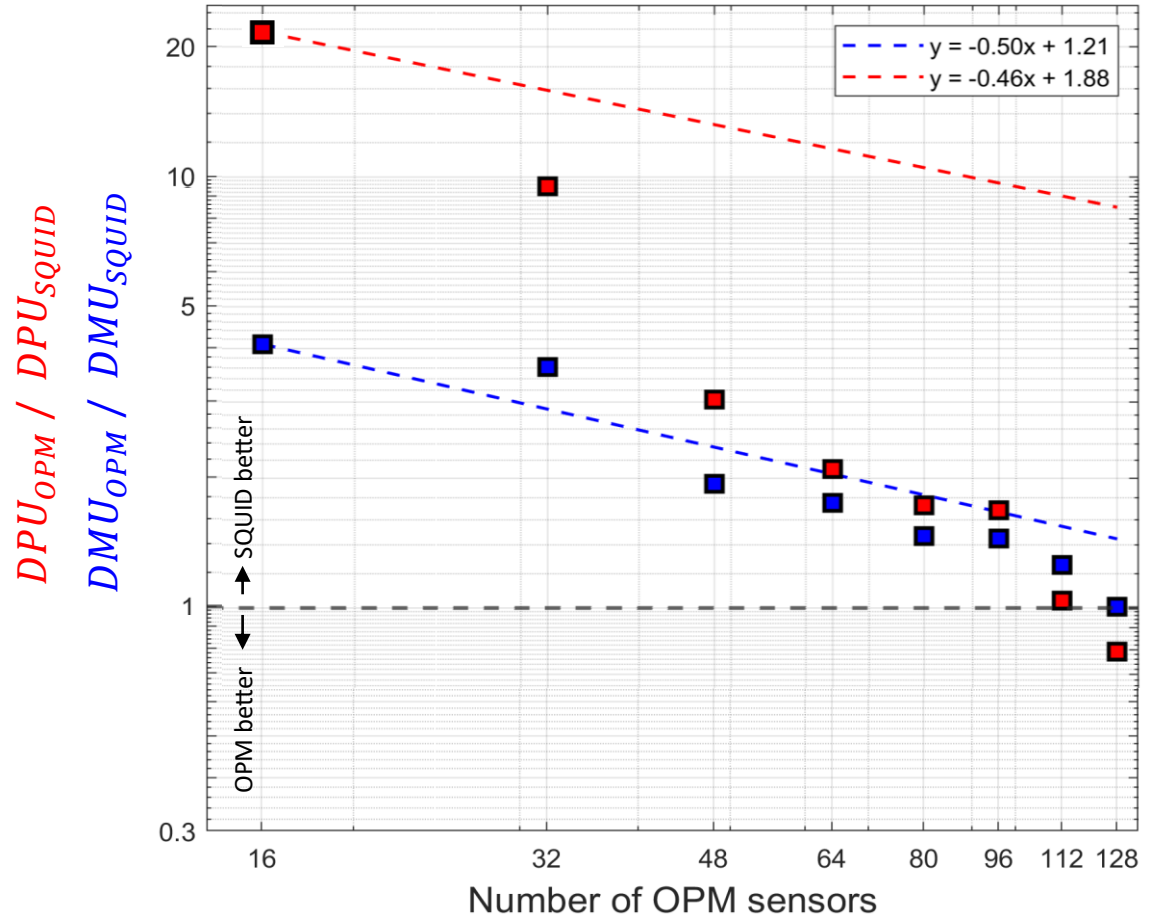


Fig. 5. Simulated data with increasing spatial resolution. The ratio of the dipole moment uncertainty (DMU; blue) and dipole position uncertainty (DPU; red) for the OPMs over the SQUIDs, plotted as a function of the number of OPM sensors. Both axes are in logarithmic scale. The dashed lines are the same as the lines fitted to the points in [figure 4B](#) with constant spatial resolution, while the square points are computed with increasing spatial resolution.

In comparison to the simulated data, which were influenced only by sensor noise and allowed for controlling of the spatial resolution, the experimental data are influenced by both sensor and environmental noise and can only have increasing spatial resolution. In [Figure 6](#) we observe for the experimental data that the improvement of DPU is more rapid than the DMU, which is in agreement with the simulated data with increasing spatial resolution ([Fig. 5](#)). Based on the DMU ratio, a system with 112 to 128 OPMs performs equally well as a system with 273 SQUIDs. Based on the DPU ratio, this number drops to 96 OPMs.

While, in the simulations, we set the sensor noise for the OPMs to be three times higher than the SQUIDs, in the experiment we cannot control the noise. To estimate the noise in the experiment, we compared the DMU ratio of the experimental data with the simulated data at three different levels of sensor noise for the OPMs ([Fig. 7](#)). We observe that for the experimental data OPM sensors seem to have two to three times more noise than the SQUIDs. In comparison to the simulations, it is challenging to determine a precise noise level for the OPMs in the experiment because each sensor has its own noise level.

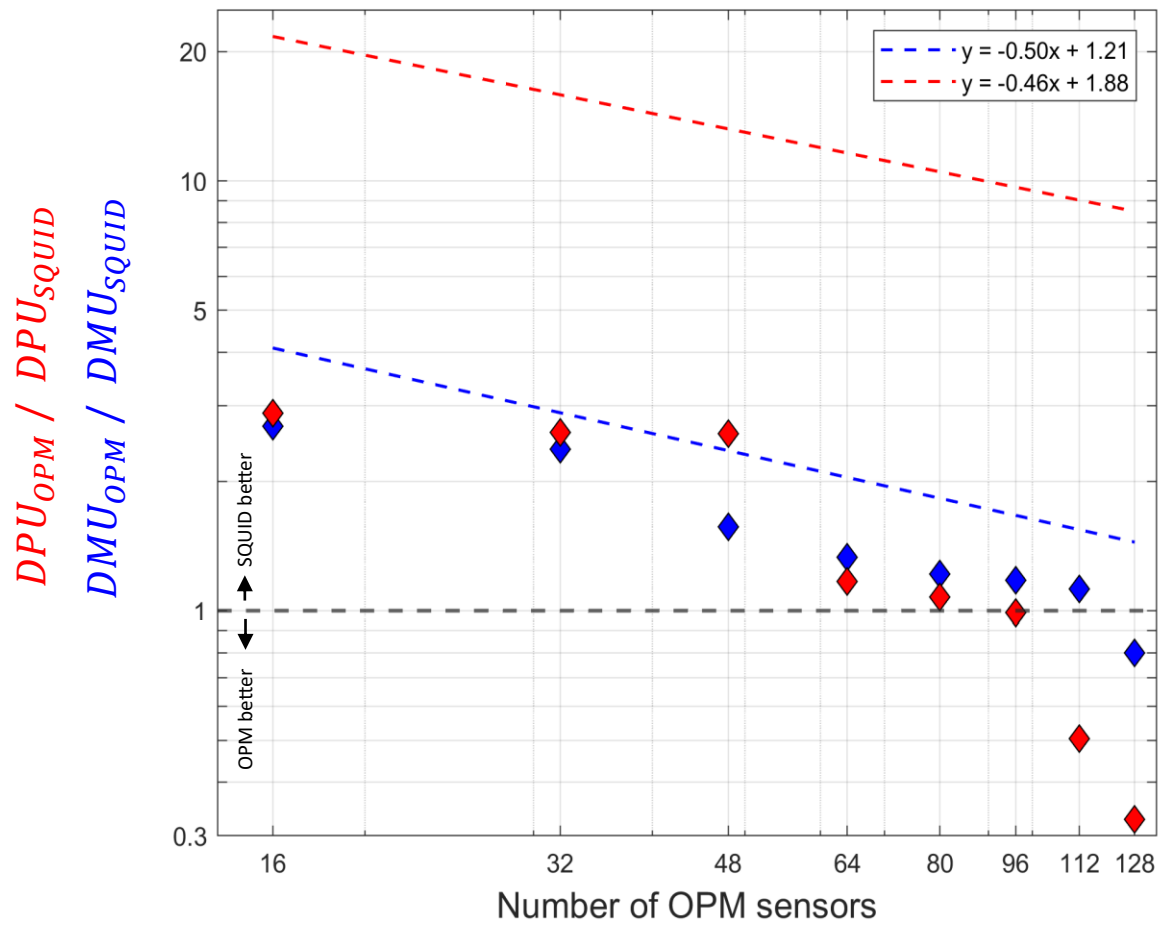


Fig. 6. Experimental data. The ratio of the dipole moment uncertainty (DMU; blue) and dipole position uncertainty (DPU; red) for the OPMs over the SQUIDs, plotted as a function of the number of OPM sensors. Both axes are in logarithmic scale. The dashed lines are the same as the lines fitted to the points in [figure 4B](#) with constant spatial resolution, while the diamond points represent the experimental data.

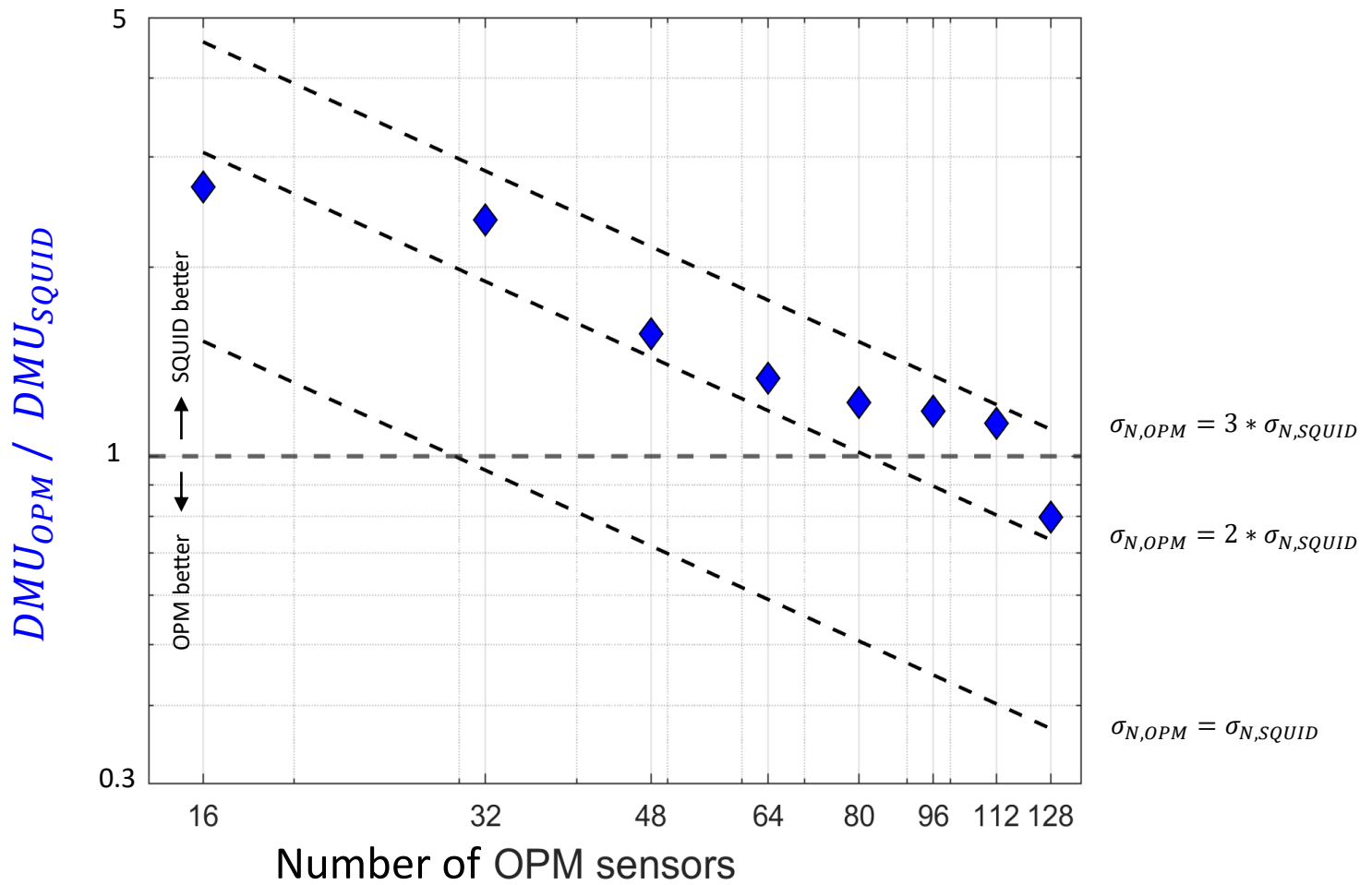


Fig. 7. Comparing experimental to simulated data with varying noise levels. Plotted in blue is the ratio of the dipole moment uncertainty (DMU) for the experimental OPM data versus the experimental SQUID data, which are the same points as in [Figure 6](#). The three dashed lines represent the simulated data with increasing spatial resolution at three noise levels: the OPM sensors are assumed to be respectively 3x, 2x, and 1x as noisy as the SQUIDs. The experimental data points fall between the dashed lines where the OPM sensors have 3x and 2x higher noise than the SQUID sensors.

To post-hoc evaluate our specification of the noise levels of the OPMs and the SQUIDs, we used the existing SQUID noise measurements that are made regularly as part of the lab quality control procedure, and we performed similar empty room recordings for the OPMs. Specifically, in the empty room recordings for the OPMs we conducted six runs identical to those in our experiment. The same sensors were placed in the same locations on the helmet for each run. Compared to the SQUIDs, the OPMs show increased noise at higher frequencies (>200 Hz) due to the limited bandwidth of the sensors and at low frequencies (<20 Hz) mainly because of environmental noise and room vibrations ([Fig. 8A](#); [Alem et al., 2023](#)). For the 20-200 Hz range, the OPMs exhibit noise levels between 10-20 fT/VHz ([Fig. 8A](#)), while SQUIDs exhibit noise levels between 4-8 fT/VHz ([Fig. 8B](#)). From our simulated data ([Fig. 5](#)) we conclude that sensors that are precise on and around the peaks of the dipolar pattern are crucial for DMU and DPU respectively. In the empty room recordings, these OPMs had noise levels of 10-15 fT/VHz (purple lines in [Fig. 8A](#)), i.e., lower than the average 10-20 fT/VHz noise levels of all the OPMs (light blue lines in [Fig. 8A](#)), whereas these SQUIDs maintained noise levels of 4-8 fT/VHz (purple lines in [Fig. 8B](#)). Consequently, the OPMs that best capture the dipolar pattern have 2-3 times higher noise than the SQUIDs (since 10-15 fT/VHz is around 2-3 times higher than 4-8 fT/VHz) which is in line with the results of [Figure 7](#).

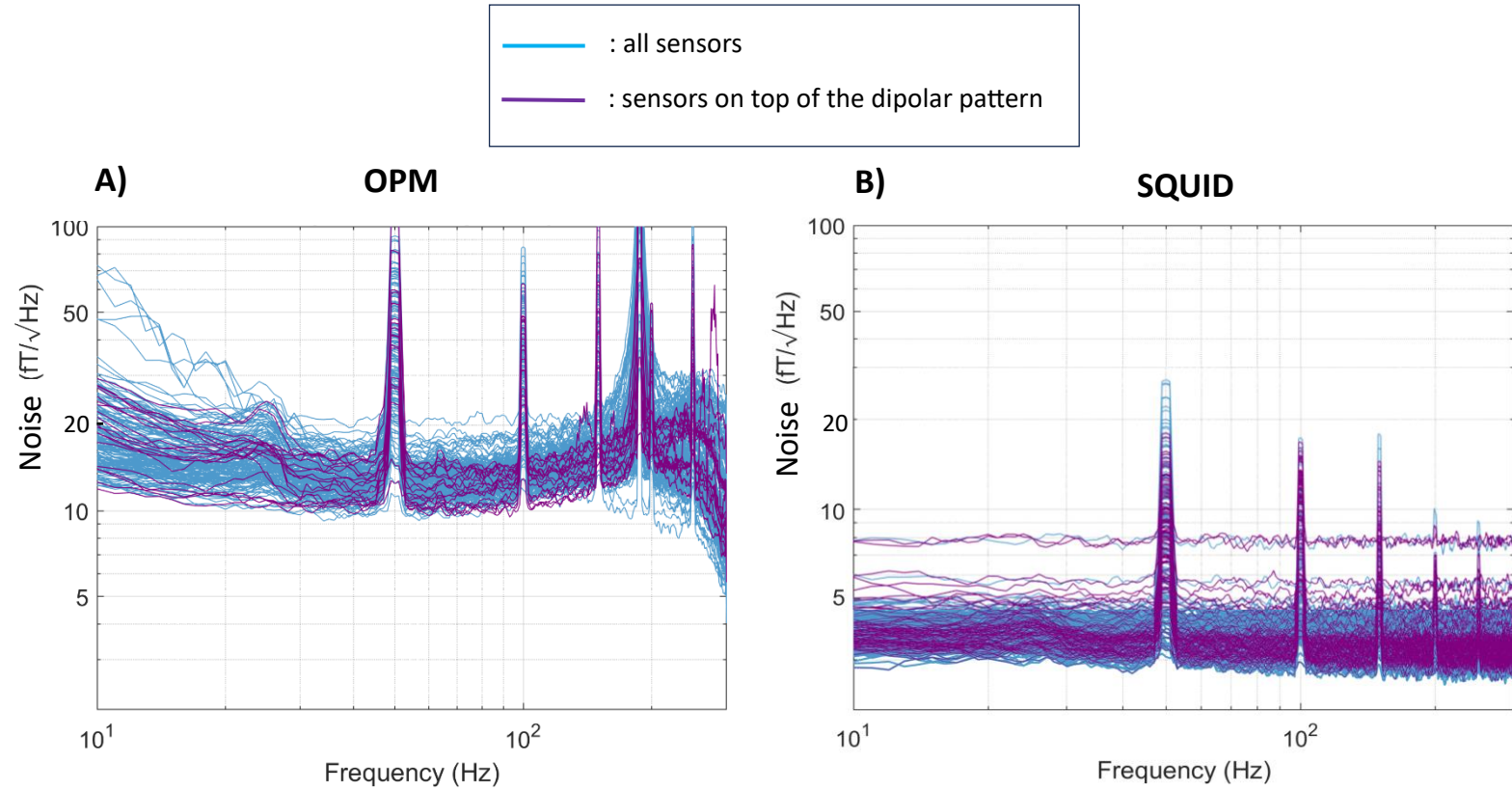


Fig. 8. Noise floors. Noise floor of the OPM magnetometers (A) and the SQUID gradiometers (B) for all the sensors (light blue) and for the sensors on top of the dipolar pattern (purple).

We performed whole-brain simulations to see how the effect of the number of OPM sensors on the DMU and DPU generalizes towards the rest of the brain. [Figure 9](#) shows the placement of the OPMs and SQUIDs for our whole-brain simulations. The upper panel displays the axial gradiometer arrangement of the 275-sensor CTF SQUID system. The sensor

positions were at least 2 cm away from the scalp. The lower panel illustrates the 144 radially oriented magnetometer arrangement for the OPM system, which is based on the FieldLine OPM helmet projected onto the scalp surface. Although in the experiment the center of the vapor cell in the FieldLine OPM sensors can be placed at minimum 5 mm from the scalp ([Alem et al., 2023](#)), for our whole-brain simulations we placed it directly on the scalp. The sensor noise of the OPMs is set to be three times higher than the SQUIDs.

[Figure 10](#) and [Figure 11](#) show the results of our whole-brain simulations with the lateral view in the top row and the medial view in the bottom row. [Figure 10](#) shows the ratio of the DMU for the two MEG systems and [Figure 11](#) the ratio of the DPU, plotted for all locations on the cortical surface. OPMs perform better than the SQUIDs for superficial brain areas, in line with the improved SNR ratio due to the close proximity of the superficial sources. In comparison to superficial sources, both the SQUID and OPM sensors pick up lower signal strength from deeper sources while the sensor noise remains identical for both superficial and deeper sources. As a result, the deeper sources have lower SNR than the superficial sources. In the temporal lobe, OPMs do not perform well, likely due to the head and brain geometry which prevents us from placing sensors close to the temporal lobe, even if we place them on the scalp. Based on the DMU ratio, a system with 128 OPMs performs equally well as a system with 275 SQUIDs for superficial brain sources, but not for deep sources. Based on the DPU ratio, this number drops to 96 OPMs. This agrees with the results from the experiment.

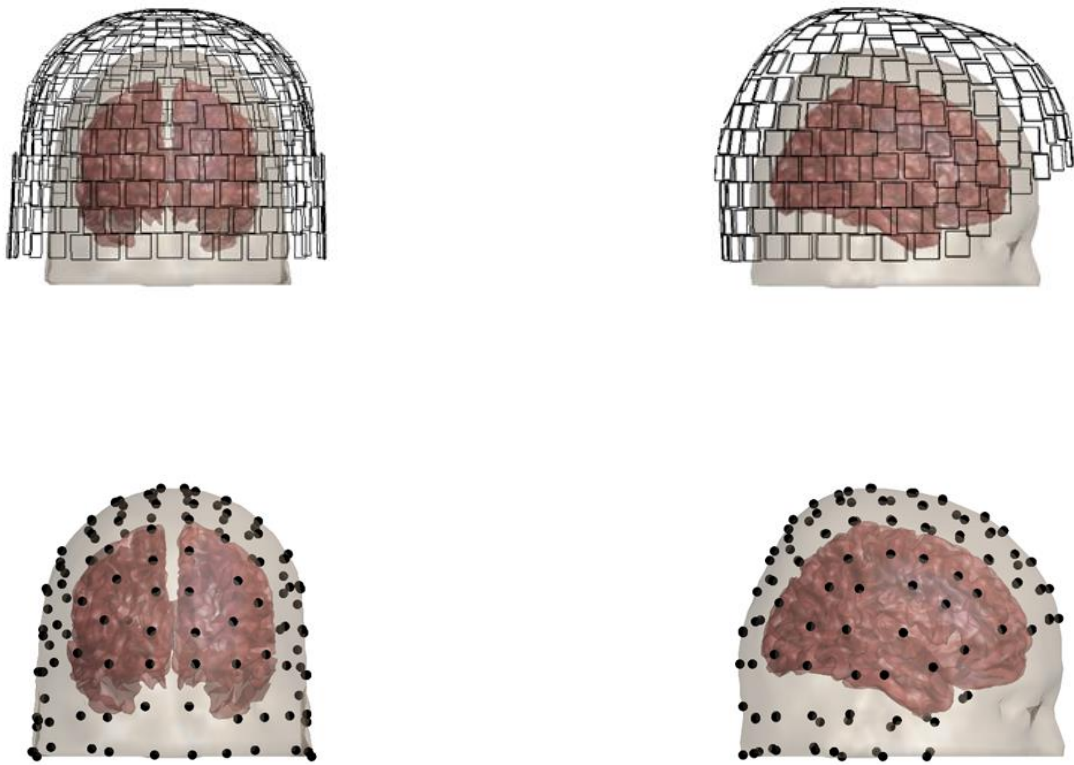


Fig. 9. Sensor placement for the whole-brain simulations. The constructed SQUID (top) and OPM (bottom) sensor positions. Frontal (left) and lateral (right) views of the sensor positions.

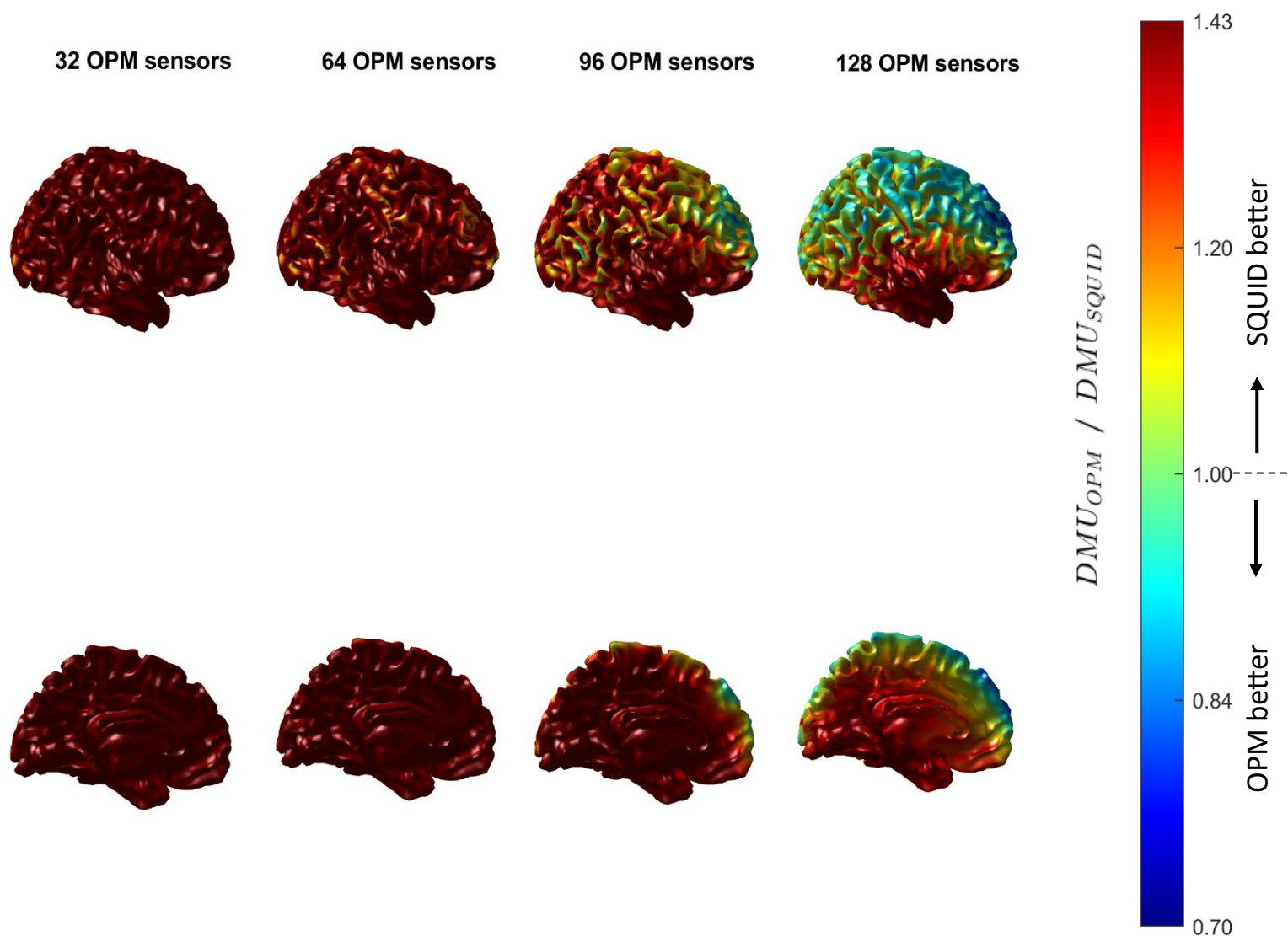


Fig. 10. DMU for whole-brain simulations. The ratio of the dipole moment uncertainty (DMU) for the OPMs over the SQUIDs, plotted as a function of dipole location in the brain. Green areas indicate an equal DMU for OPMs and SQUIDs. Areas coloured blue indicate that the DMU of the OPMs is lower than the SQUIDs, suggesting better performance for OPMs. Conversely, red areas indicate that the DMU of the OPMs is higher than the SQUIDs, suggesting better performance for SQUIDs. The number of OPM sensors varies from 32, 64,

96 to 128. The lateral view of the brain (top) highlights the superficial parts of the brain while the medial view (bottom) the deeper ones.

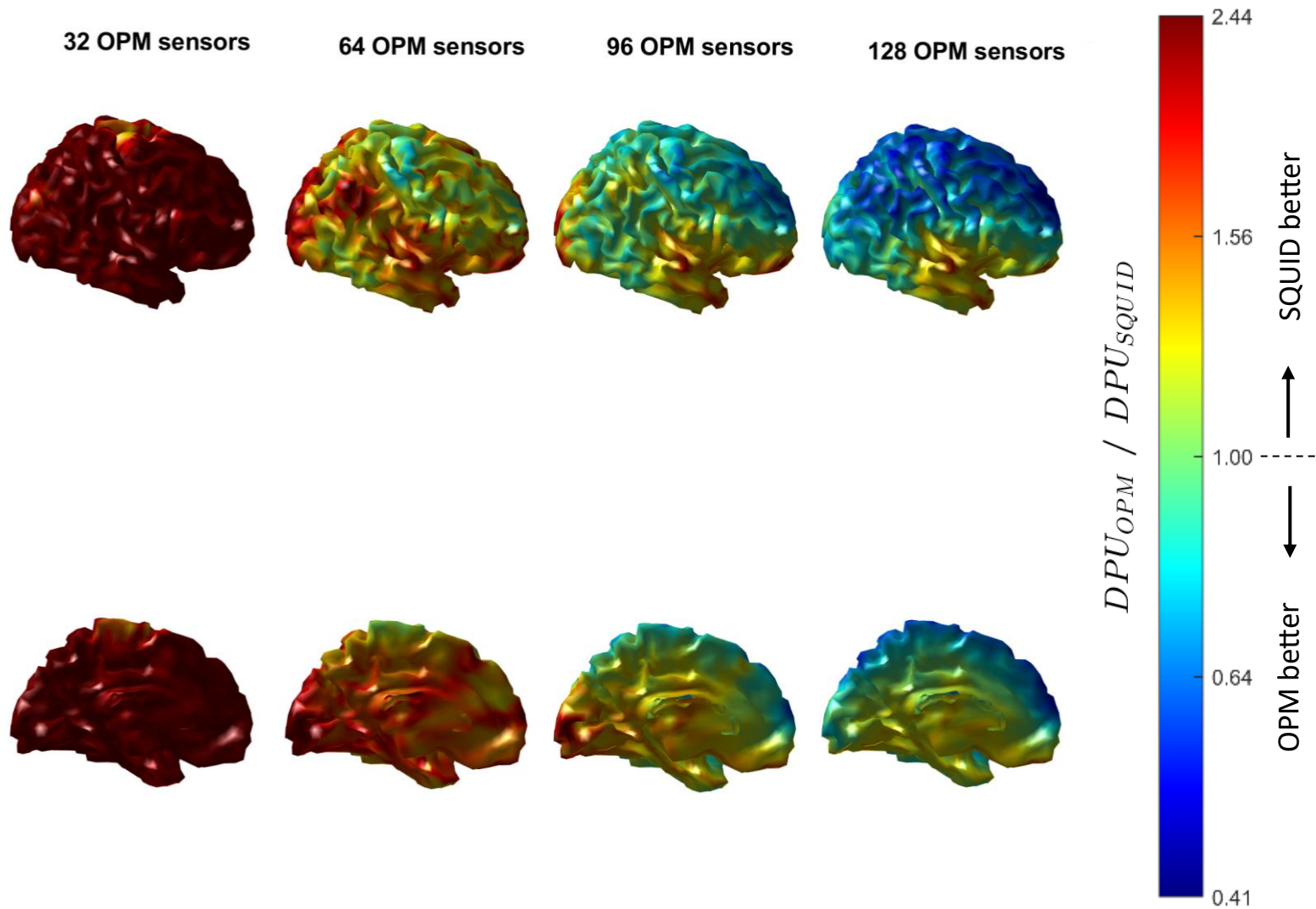


Fig. 11. DPU for whole brain simulations. The ratio of the dipole position uncertainty (DPU) for the OPMs over the SQUIDs, plotted as a function of dipole location in the brain. Green areas indicate an equal DPU for OPMs and SQUIDs. Areas coloured blue indicate that the DPU of the OPMs is lower than the SQUIDs, suggesting better performance for OPMs.

Conversely, red areas indicate that the DPU of the OPMs is higher than the SQUIDs, suggesting better performance for SQUIDs. The number of OPM sensors varies from 32, 64, 96 to 128. The lateral view of the brain (top) highlights the superficial parts of the brain while the medial view (bottom) the deeper ones.

4 Discussion

The aim of the research described in this master's thesis is to answer the question how many sensors are required for an OPM system to achieve similar dipole moment uncertainty (DMU) and dipole position uncertainty (DPU) as with the 275-sensor CTF SQUID system. This was investigated using an experiment with left median nerve stimulation, validated by a simulation of a dipole at the corresponding right S1 area and further generalized towards the rest of the brain. As the starting point for our simulations we assumed OPMs to have 3 times the noise of SQUIDs, however our experimental results show that OPMs are only 2 to 3 times noisier than SQUIDs. Based on these results we conclude that a system with 112-128 OPMs has an equal dipole moment uncertainty (DMU) to a system with 275 SQUIDs. Additionally, a system with around 96 OPMs has equal dipole position uncertainty (DPU) to a system with 275 SQUIDs. These results apply to a superficial source in the right S1 area but do not extend to deeper regions. The relative SNR benefit of OPMs due to the stronger signal of superficial cortical sources (compared to the SQUIDs) does not apply to deeper sources since for these regions both OPMs and SQUIDs are relatively far away.

To determine the required number of sensors for an OPM system, we investigated two different ways of quantifying the source reconstruction accuracy. Our simulations with constant spatial resolution showed that both DMU and DPU decreased with the square root

of the number of OPM sensors ([Fig. 4](#)). For realistic sensor placements, the dependence of DMU and DPU on the number of sensors is not straightforward; increasing the number of sensors increases also the sensor coverage and the spatial resolution of the OPM system (see [section 2.1.3](#)). Both the experiment and the increasing spatial resolution in simulations showed that DPU decreased more rapidly than the DMU as the number of sensors increased. This is relevant for applications where the position of a focal source is important, for example clinicians investigating epileptic patients. Having high spatial resolution (i.e., a high-density OPM array) decreases rapidly the DPU, facilitating the clinicians to find and remove the source of the epileptic seizures. An advantage of the OPMs is the flexibility to redistribute sensors in the helmet which allows to strategically target brain regions of interest ([Nugent et al., 2022](#)). [Hill et al. \(2024\)](#) showed that strategically targeting brain regions of interest with OPMs can increase the SNR. In epilepsy treatment strategic sensor placement is possible following localisation with EEG or MRI of the regions potentially causing seizures. By combining high spatial resolution with strategic sensor placement, we can achieve significant improvements in DPU.

Our analytic solution demonstrated that DMU is proportional to the standard deviation of the sensor noise and inversely proportional to the norm of the forward field $||L||$ ([section 2.5.1](#), Eq. (8)). DMU benefits from placing sensors at the peaks of the dipolar pattern, where the norm of the forward field $||L||$ is the largest. Although increasing the spatial resolution results in some sensors being closer to the peaks, only a few of them can cover the peaks (which in our case is limited by how close the sensors are placed to each other). To further decrease the DMU, it is essential to reduce sensor noise. As shown in [Figure 7](#), decreasing the OPM sensor noise from 3 to 1 time that of SQUIDs would reduce the number of OPM sensors needed to perform equally well for a superficial source as the 275-sensor CTF SQUID system from 128 to approximately 32. DPU also depends on sensor noise; however, it is less critical because DPU benefits more than DMU from an increasing spatial resolution.

Therefore, cognitive scientists that aim to design experiments that contrast the SNR of the neural activity between different experimental conditions are likely to benefit relative more from OPMs with lower sensor noise than clinicians that aim to localize epileptiform activity.

The higher noise of the OPM sensors is partially compensated by the closer placement to the brain and can partially be compensated by increasing the number of OPM sensors. OPMs perform well on superficial brain areas, but not as well in deeper areas and the temporal lobe. These regions are far from the SQUIDs and also remain relatively far from the OPMs, resulting in lower signal strength being picked up. As shown in [Figure 10](#) and [11](#), a system with 275 SQUIDs has a higher source reconstruction accuracy than a system with 128 OPMs for deeper areas and the temporal lobe. Lowering the sensor noise of the OPMs would benefit research into deeper structures, such as detection of hippocampal epileptiform activity ([Hillebrand et al., 2023](#)) or understanding the subcortical contributions and their interaction with cortical areas to balance and gait ([Nonnekes et al., 2015](#)).

More sensors not only improve source reconstruction accuracy ([Fig. 4](#)), but also allow denoising techniques such as homogeneous field correction (HFC) ([Tierney et al., 2021](#)) or adaptive multipole models ([Tierney et al., 2023](#)) to spatially separate brain signal and environmental noise. Consequently, we can perform better denoising of environmental noise, to which OPMs as magnetometers are more sensitive than the SQUID gradiometers. Specifically, adaptive multipole models require a minimum of 150 sensors, since the number of sensors needs to be greater than the number of harmonics modelled ([Tierney et al., 2022](#)).

During our experiment our OPM sensors remained well within their dynamic range in our MSR without requiring nulling coils for static or dynamic noise cancellation. This was due to two factors: first, our OPM sensors operate in closed-loop which provides a higher dynamic range compared to open-loop operation ([Alem et al., 2023](#)); second, we mounted

the helmet on a wooden plate, which prevented movement artifacts and non-linearities in the signal. In the future as we aim to utilize the full potential of OPMs, it remains to be seen whether the OPMs will remain within their dynamic range also in experiments that allow movements. If they were to exceed the dynamic range, we need to perform static and dynamic noise cancellation using Helmholtz ([Ivanainen et al., 2019](#)) or matrix coils ([Holmes et al., 2023](#)) during the data acquisition. Furthermore, for MEG experiments in which the sensors move we need to capture those movements and remove the motion artifacts post-acquisition ([Seymour et al., 2021](#)).

A limitation of our study is that our current OPM system is limited to 32 sensors, so to obtain a measurement for each slot, we divided the experiment into six runs. During data analysis, we combined these six runs to represent a single experiment with 144 sensors. To clean the data, we performed a separate HFC for each run. Since each run had different environmental noise levels, the noise in the data after cleaning varied between runs. Consequently, when combining these runs to represent a single experiment, we have varying noise levels in the combined data. Moreover, several factors could affect the neural activity between runs. These include participant fatigue (which can increase the alpha band activity over the occipital and parietal lobes), stimulator shifts due to sweat or hand movements, and possible desensitization of the nerve after repeated stimulations.

Another limitation is that in our experiment we tested only specific sensors in specific locations on the scalp. [Figure 8](#) demonstrates that OPM sensors have noise levels between 10-20 fT/VHz while SQUIDs have noise levels between 4-8 fT/VHz. This suggests that OPMs can be approximately 2 to 4 times noisier than SQUIDs. Additionally, based on [Figure 5](#), we concluded that sensors placed on top of the dipolar pattern are crucial for the performance of the OPMs. Therefore, since we only tested specific sensors in specific locations on the scalp, it was possible for the sensors placed on top of the dipolar pattern to be either among

the noisiest or among the least noisy. [Figure 8A](#) demonstrates that the noise of the OPM sensors placed on top of the dipolar pattern (10-15 fT/VHz) is lower than the average noise levels of all the OPMs (10-20 fT/VHz). Hence it appears that we were lucky in selecting the least noisy OPM sensors to be placed on top of the dipolar pattern. Thus, the number of sensors for an OPM system to perform equally well as the 275-sensor CTF SQUID system may be slightly higher than what our experiment suggested.

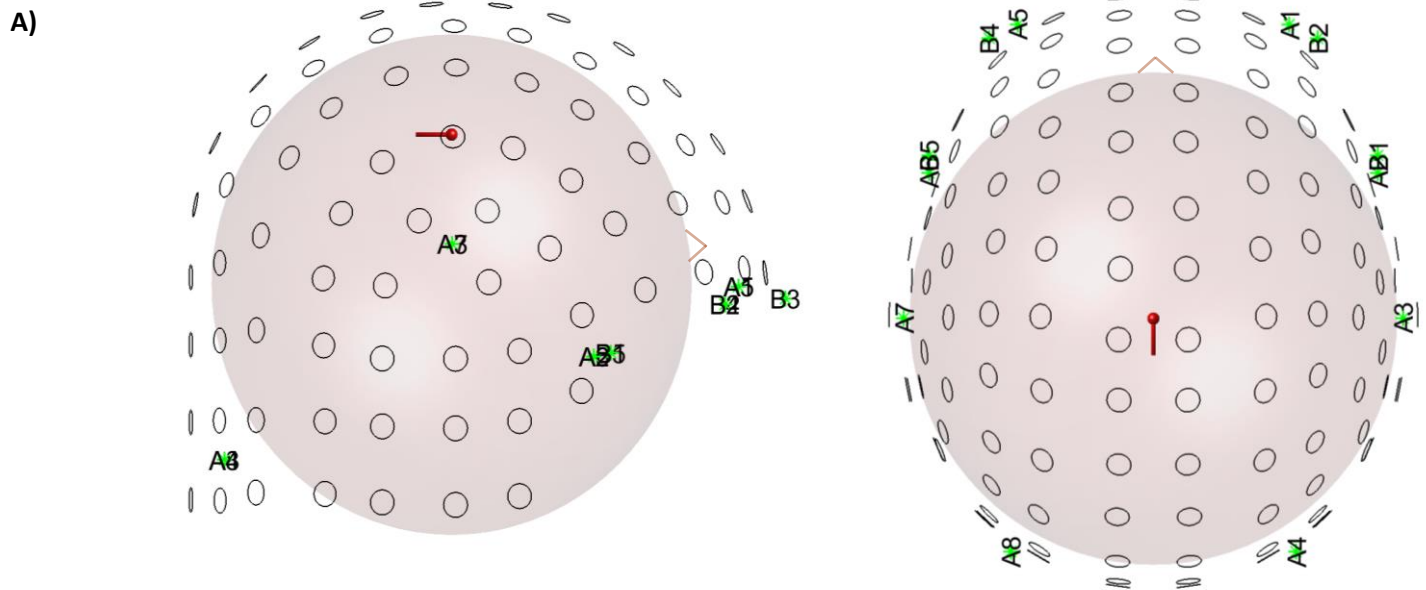
5 Conclusion

In conclusion, our study suggests that for a source at the right S1 area, a system with 128 OPMs can have higher source reconstruction accuracy compared to the 275-sensor CTF SQUID system. However, the required number of OPM sensors can vary depending on whether the focus is on the dipole position or dipole moment (or neural activity strength). Dipole position benefits from placing the sensors closer to each other. Dipole moment benefits less from placing the sensors closer to each other and as a result it is more impacted from the increased sensor noise of the OPMs in comparison to the SQUIDs. We also demonstrated that OPMs perform better than SQUIDs on superficial brain areas, but not as well in deeper areas as they are far from the sensors resulting in lower signal strength being picked up. As OPMs are increasingly adopted by clinical and neuroscience research institutes, including the Donders Institute, it is important to recognize that the optimal number of OPM sensors required can vary based on the research question (whether it investigates the position or strength of neural activity) and the brain regions of interest (superficial or deeper brain areas). Additionally, we would benefit from future improvements in OPM sensor technology, such as lower sensor noise and OPM arrays that allow sensors to be placed closer to each other.

6 Data and code availability

All data were acquired by the authors and are available in the Donders repository. All code was developed using MATLAB and is available in GitHub.

7 Supplementary material



B)

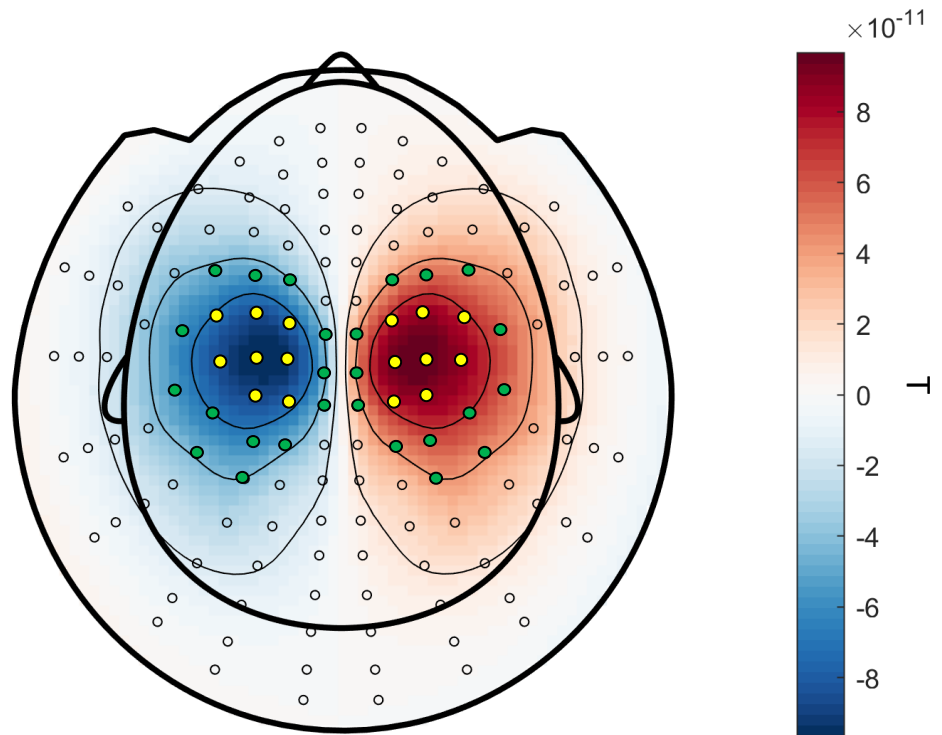


Figure A1. Effect of sensor location on source reconstruction accuracy. A) Simple simulation using a single sphere volume conduction model. Data are simulated from a single dipole placed in the center of the head (dipole position is [0, 0, 60] mm) and oriented towards the posterior of the head (dipole moment is [0, -0.01, 0] A * m). The FieldLine OPM system (Boulder, Colorado) which has 144 radially-oriented OPM sensors is also depicted. B) Field patterns as recorded with the FieldLine OPM system. Yellow sensors are closer to the peaks of the dipolar pattern, leading to a rapid decrease of dipole moment uncertainty (DMU). Green sensors capture better the gradients of the dipolar pattern (i.e., areas around the peaks), resulting in a rapid decrease dipole position uncertainty (DPU).

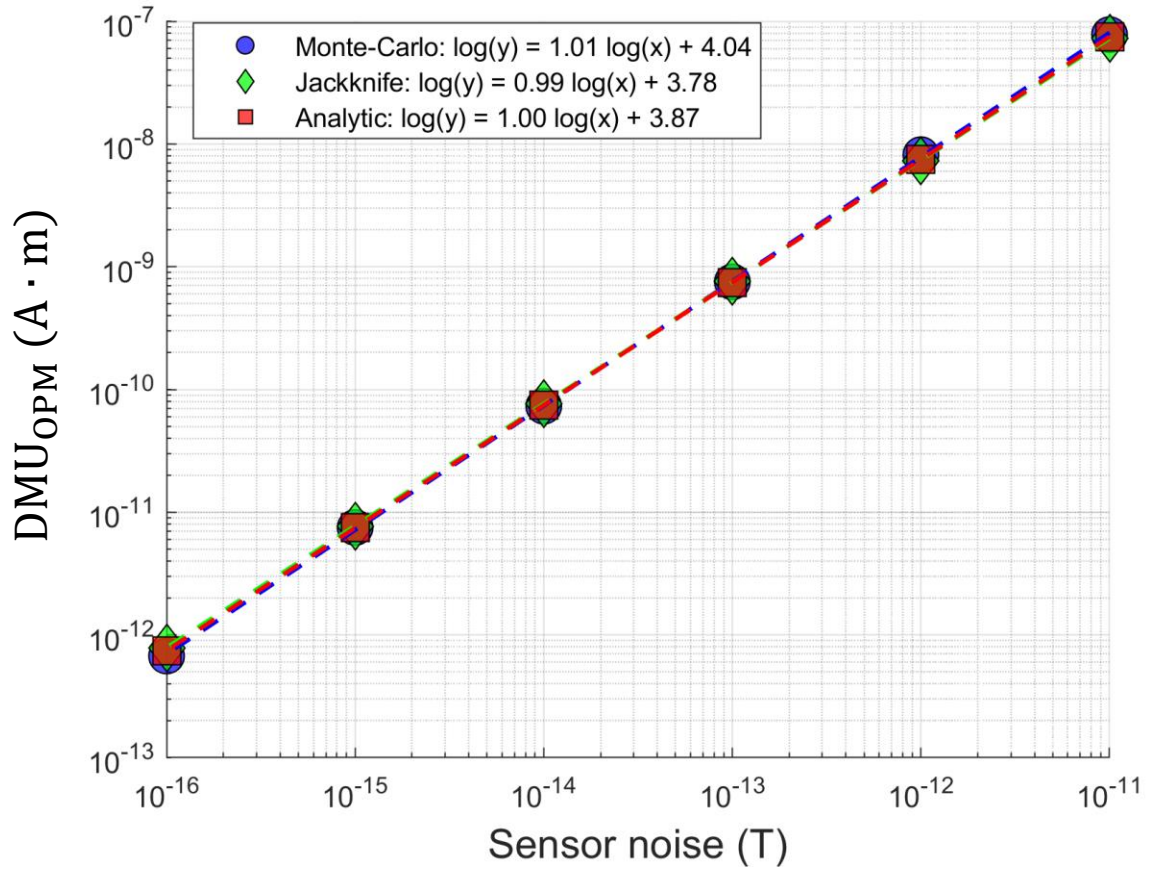
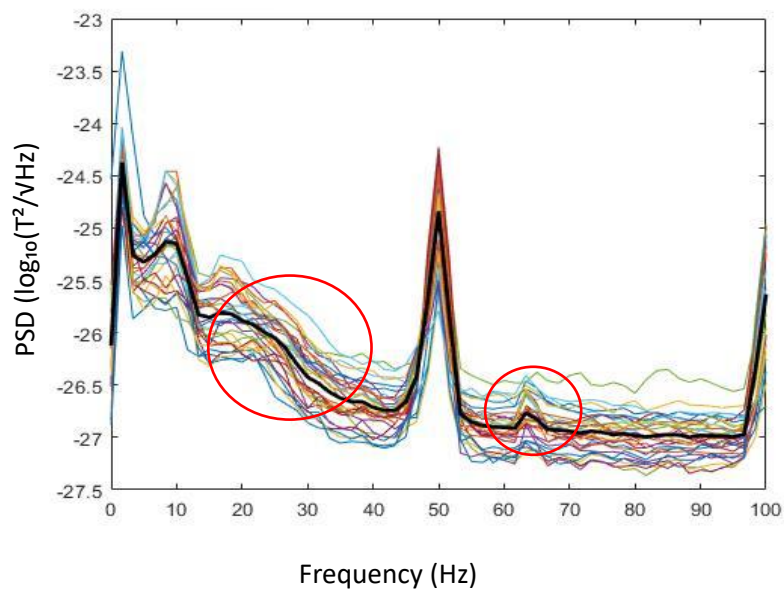


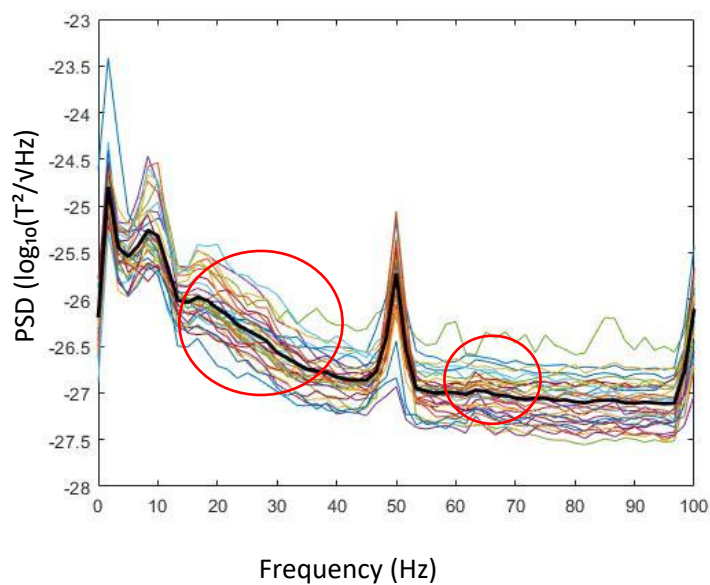
Figure A2. Analytic solution, jackknife resampling and Monte Carlo simulations. The dipole moment uncertainty (DMU) for the OPMs is plotted as a function of Gaussian sensor noise. The analytic solution (red squares), jackknife resampling (green diamonds), and Monte Carlo simulations (blue circles) yield the same DMU values across different noise levels. Hence, these three methods are directly comparable and can be used interchangeably. A line is fitted to each set of points. For the jackknife resampling (green diamonds), and Monte Carlo simulations (blue circles) this fitted line has slope of 1, confirming our analytic solution that DMU and sensor noise are proportional, as shown in [Section 2.5.1](#), Eq. (8).

A) Subject001

No HFC applied

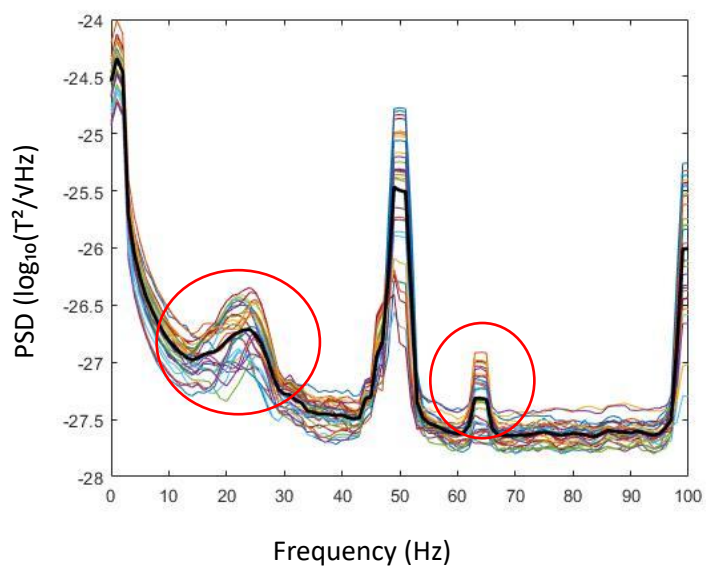


HFC applied



B) Empty room recording

No HFC applied



HFC applied

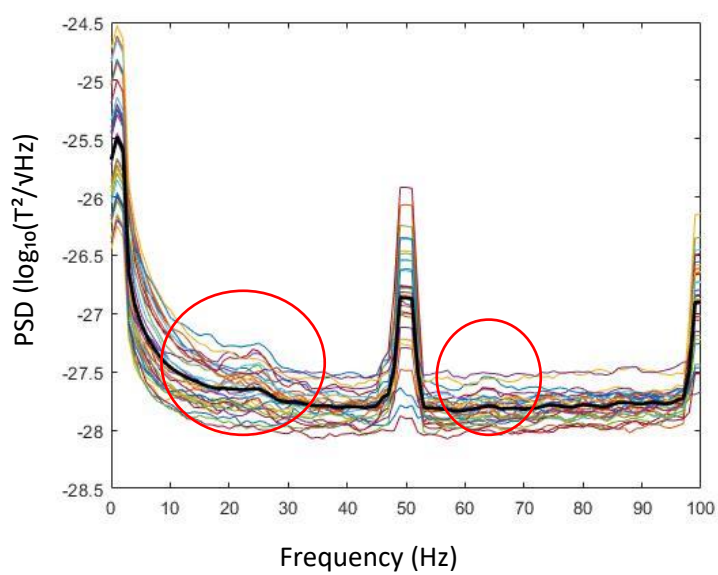
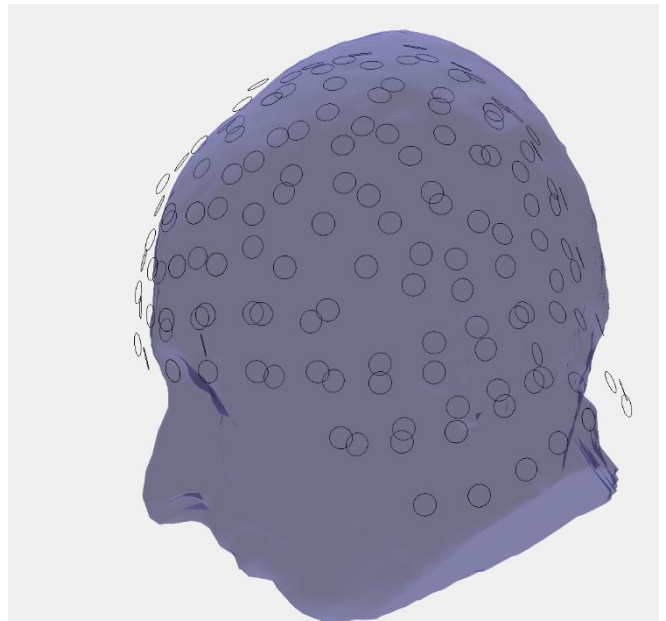
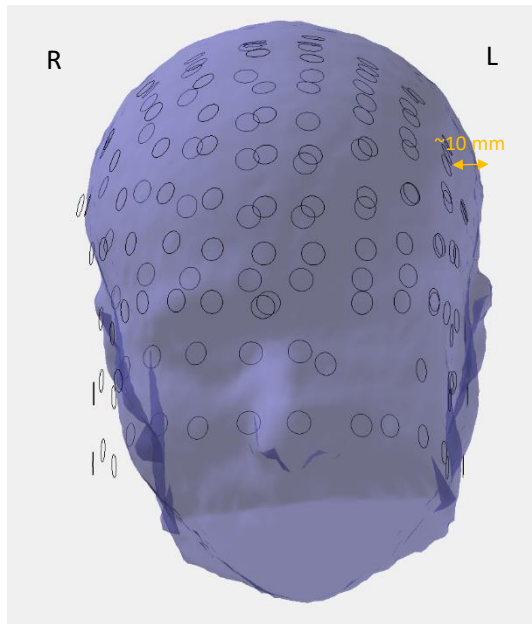
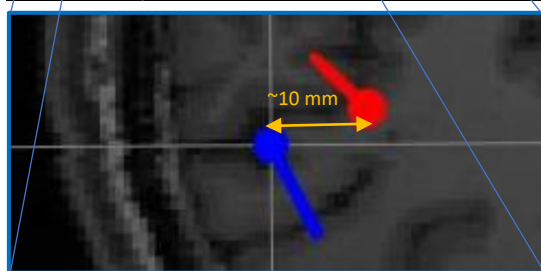
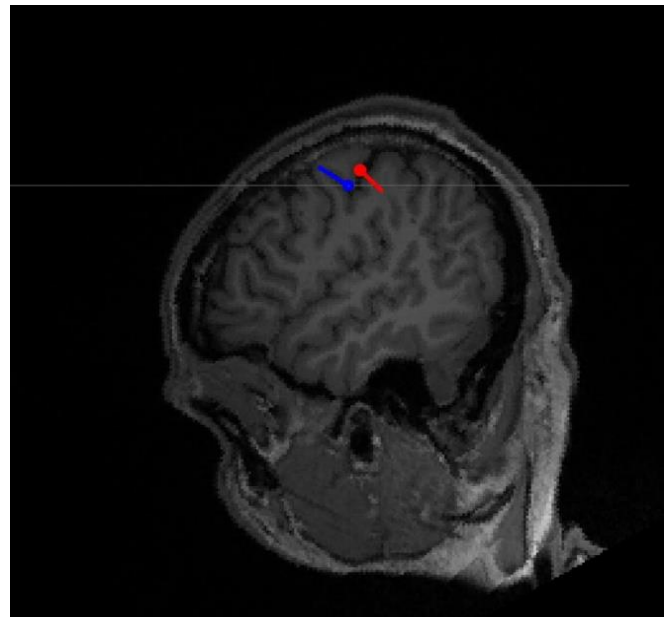
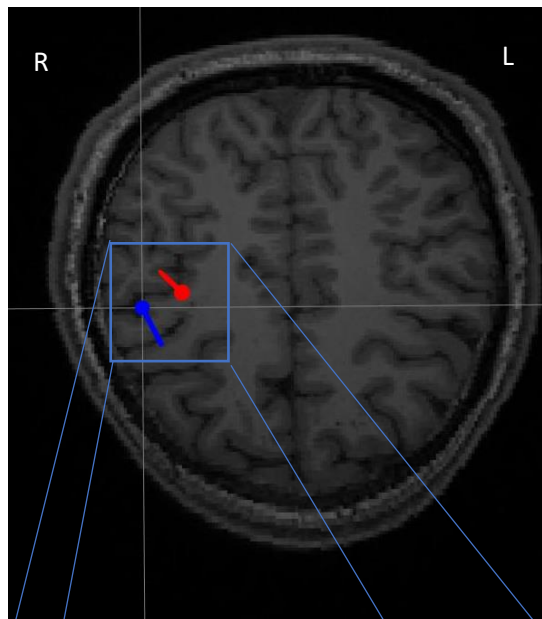


Figure A3. Homogeneous field correction (HFC). HFC successfully reduces magnetic interference in OPM magnetometers. It reduces low-frequency environmental noise and potential noise in the ~60-70 Hz range, as shown in both the experiment (A) and empty room recordings (B).

A)



B)



● : Dipole fitted from OPM data

● : Dipole fitted from SQUID data

Figure A4. Dipole fits 20 ms post-stimulation based on OPM (blue) and SQUID (red) MEG recordings. A) The co-registration using a 3D scan was not totally accurate causing the OPM sensors to shift towards the right. B) As a result, the dipole in the OPM measurements (blue) shifted towards the right relative to the SQUID measurements (red). The distance between the two dipoles was approximately 10 mm.

8 References

- Alem, O., Hughes, K. J., Buard, I., Cheung, T. P., Maydew, T., Griesshammer, A., Holloway, K., Park, A., Lechuga, V., Coolidge, C., Gerginov, M., Quigg, E., Seames, A., Kronberg, E., Teale, P., & Knappe, S. (2023). An integrated full-head OPM-MEG system based on 128 zero-field sensors. *Frontiers in Neuroscience*, 17, 1190310.
<https://doi.org/10.3389/fnins.2023.1190310>
- Andersen, L. M., & Dalal, S. S. (2021). The cerebellar clock: Predicting and timing somatosensory touch. *NeuroImage*, 238, 118202.
<https://doi.org/10.1016/j.neuroimage.2021.118202>
- Baillet, S., Mosher, J., & Leahy, R. (2001). Electromagnetic brain mapping. *Signal Processing Magazine, IEEE*, 18, 14-30. <https://doi.org/10.1109/79.962275>
- Boto, E., Bowtell, R., Krüger, P., Fromhold, T. M., Morris, P. G., Meyer, S. S., Barnes, G. R., & Brookes, M. J. (2016). On the Potential of a New Generation of Magnetometers for MEG: A Beamformer Simulation Study. *PloS one*, 11(8), e0157655.
<https://doi.org/10.1371/journal.pone.0157655>

- Boto, E., Holmes, N., Leggett, J., Roberts, G., Shah, V., Meyer, S. S., Muñoz, L. D., Mullinger, K. J., Tierney, T. M., Bestmann, S., Barnes, G. R., Bowtell, R., & Brookes, M. J. (2018). Moving magnetoencephalography towards real-world applications with a wearable system. *Nature*, 555(7698), 657–661. <https://doi.org/10.1038/nature26147>
- Boto, E., Meyer, S. S., Shah, V., Alem, O., Knappe, S., Kruger, P., Fromhold, T. M., Lim, M., Glover, P. M., Morris, P. G., Bowtell, R., Barnes, G. R., & Brookes, M. J. (2017). A new generation of magnetoencephalography: Room temperature measurements using optically-pumped magnetometers. *NeuroImage*, 149, 404–414. <https://doi.org/10.1016/j.neuroimage.2017.01.034>
- Brookes, M. J., Boto, E., Rea, M., Shah, V., Osborne, J., Holmes, N., Hill, R. M., Leggett, J., Rhodes, N., & Bowtell, R. (2021). Theoretical advantages of a triaxial optically pumped magnetometer magnetoencephalography system. *NeuroImage*, 236, 118025. <https://doi.org/10.1016/j.neuroimage.2021.118025>
- Brookes, M. J., Leggett, J., Rea, M., Hill, R. M., Holmes, N., Boto, E., & Bowtell, R. (2022). Magnetoencephalography with optically pumped magnetometers (OPM-MEG): The next generation of functional neuroimaging. *Trends in Neurosciences*, 45(8), 621–634. <https://doi.org/10.1016/j.tins.2022.05.008>
- Buchner, H., Fuchs, M., Wischmann, H.-A., Dössel, O., Ludwig, I., Knepper, A., & Berg, P. (1994). Source analysis of median nerve and finger stimulated somatosensory evoked potentials: Multichannel simultaneous recording of electric and magnetic fields combined with 3d-MR tomography. *Brain Topography*, 6(4), 299–310. <https://doi.org/10.1007/BF01211175>
- Cockx, H. M., Oostenveld, R., Flórez R, Y. A., Bloem, B. R., Cameron, I. G. M., & Van Wezel, R. J. A. (2024). Freezing of gait in Parkinson’s disease is related to imbalanced

stopping-related cortical activity. *Brain Communications*, fcae259.

<https://doi.org/10.1093/braincomms/fcae259>

Corvilain, P., Wens, V., Bourguignon, M., Capparini, C., Fourdin, L., Ferez, M., Feys, O., De

Tiège, X., & Bertels, J. (2023). Extending the applicability of optically pumped magnetoencephalography toward early human life. *bioRxiv*.

<https://doi.org/10.1101/2023.10.28.564455>

Cruse, D., Beukema, S., Chennu, S., Malins, J. G., Owen, A. M., & McRae, K. (2014). The reliability of the N400 in single subjects: implications for patients with disorders of consciousness. *NeuroImage. Clinical*, 4, 788–799.

<https://doi.org/10.1016/j.nicl.2014.05.001>

Fred, A. L., Kumar, S. N., Kumar Haridhas, A., Ghosh, S., Purushothaman Bhuvana, H., Sim,

W. K. J., Vimalan, V., Givo, F. A. S., Jousmäki, V., Padmanabhan, P., & Gulyás, B.

(2022). A Brief Introduction to Magnetoencephalography (MEG) and Its Clinical

Applications. *Brain sciences*, 12(6), 788. <https://doi.org/10.3390/brainsci12060788>

Hill, R. M., Boto, E., Rea, M., Holmes, N., Leggett, J., Coles, L. A., Papastavrou, M., Everton, S.

K., Hunt, B. A. E., Sims, D., Osborne, J., Shah, V., Bowtell, R., & Brookes, M. J. (2020).

Multi-channel whole-head OPM-MEG: Helmet design and a comparison with a conventional system. *NeuroImage*, 219, 116995.

<https://doi.org/10.1016/j.neuroimage.2020.116995>

Hill, R. M., Devasagayam, J., Holmes, N., Boto, E., Shah, V., Osborne, J., Safar, K., Worcester,

F., Mariani, C., Dawson, E., Woolger, D., Bowtell, R., Taylor, M. J., & Brookes, M. J.

(2022). Using OPM-MEG in contrasting magnetic environments. *NeuroImage*, 253,

119084. <https://doi.org/10.1016/j.neuroimage.2022.119084>

Hill, R. M., Schofield, H., Boto, E., Rier, L., Osborne, J., Doyle, C., Worcester, F., Hayward, T., Holmes, N., Bowtell, R., Shah, V., & Brookes, M. J. (2024). Optimising the sensitivity of optically-pumped magnetometer magnetoencephalography to gamma band electrophysiological activity. *Imaging Neuroscience*, 2, 1–19.
https://doi.org/10.1162/imag_a_00112

Hillebrand, A., Holmes, N., Sijsma, N., O'Neill, G. C., Tierney, T. M., Liberton, N., Stam, A. H., van Klink, N., Stam, C. J., Bowtell, R., Brookes, M. J., & Barnes, G. R. (2023). Non-invasive measurements of ictal and interictal epileptiform activity using optically pumped magnetometers. *Scientific reports*, 13(1), 4623.
<https://doi.org/10.1038/s41598-023-31111-y>

Holmes, C. J., Hoge, R., Collins, L., Woods, R., Toga, A. W., & Evans, A. C. (1998). Enhancement of MR Images Using Registration for Signal Averaging: *Journal of Computer Assisted Tomography*, 22(2), 324–333.
<https://doi.org/10.1097/00004728-199803000-00032>

Holmes, N., Rea, M., Hill, R. M., Leggett, J., Edwards, L. J., Hobson, P. J., Boto, E., Tierney, T. M., Rier, L., Rivero, G. R., Shah, V., Osborne, J., Fromhold, T. M., Glover, P., Brookes, M. J., & Bowtell, R. (2023). Enabling ambulatory movement in wearable magnetoencephalography with matrix coil active magnetic shielding. *NeuroImage*, 274, 120157. <https://doi.org/10.1016/j.neuroimage.2023.120157>

Iivanainen, J., Stenroos, M., & Parkkonen, L. (2017). Measuring MEG closer to the brain: Performance of on-scalp sensor arrays. *NeuroImage*, 147, 542–553.
<https://doi.org/10.1016/j.neuroimage.2016.12.048>

- Iivanainen, J., Zetter, R., Grön, M., Hakkarainen, K., & Parkkonen, L. (2019). On-scalp MEG system utilizing an actively shielded array of optically-pumped magnetometers. *NeuroImage*, 194, 244–258. <https://doi.org/10.1016/j.neuroimage.2019.03.022>
- Ilmoniemi, R. J., Hamalainen, M. S., & Knuutila, J. (1985). The forward and inverse problems in the spherical model. In H. Weinberg, G. Stroink, & H. Katila. *Biomagnetism: Application*, 278-282.
- Mellor, S., Tierney, T. M., Seymour, R. A., Timms, R. C., O'Neill, G. C., Alexander, N., Spedden, M. E., Payne, H., & Barnes, G. R. (2023). Real-time, model-based magnetic field correction for moving, wearable MEG. *NeuroImage*, 278, 120252. <https://doi.org/10.1016/j.neuroimage.2023.120252>
- Metropolis, N., & Ulam, S. (1949). The Monte Carlo Method. *Journal of the American Statistical Association*, 44(247), 335–341. <https://doi.org/10.1080/01621459.1949.10483310>
- Mosher, J. C., Leahy, R. M., & Lewis, P. S. (1999). EEG and MEG: Forward solutions for inverse methods. *IEEE Transactions on Biomedical Engineering*, 46(3), 245–259. <https://doi.org/10.1109/10.748978>
- Nonnekes, J., Carpenter, M. G., Inglis, J. T., Duysens, J., & Weerdesteyn, V. (2015). What startles tell us about control of posture and gait. *Neuroscience & Biobehavioral Reviews*, 53, 131–138. <https://doi.org/10.1016/j.neubiorev.2015.04.002>
- Nugent, A. C., Benitez Andonegui, A., Holroyd, T., & Robinson, S. E. (2022). On-scalp magnetocorticography with optically pumped magnetometers: Simulated performance in resolving simultaneous sources. *Neuroimage: Reports*, 2(2), 100093. <https://doi.org/10.1016/j.ynirp.2022.100093>

Oostenveld, R., Fries, P., Maris, E., & Schoffelen, J. M. (2011). FieldTrip: Open source software for advanced analysis of MEG, EEG, and invasive electrophysiological data. *Computational intelligence and neuroscience*, 2011, 156869.

<https://doi.org/10.1155/2011/156869>

Quenouille, M. H. (1956). NOTES ON BIAS IN ESTIMATION. *Biometrika*, 43(3–4), 353–360.

<https://doi.org/10.1093/biomet/43.3-4.353>

Seymour, R. A., Alexander, N., Mellor, S., O'Neill, G. C., Tierney, T. M., Barnes, G. R., & Maguire, E. A. (2021). Using OPMs to measure neural activity in standing, mobile participants. *NeuroImage*, 244, 118604.

<https://doi.org/10.1016/j.neuroimage.2021.118604>

Seymour, R. A., Alexander, N., Mellor, S., O'Neill, G. C., Tierney, T. M., Barnes, G. R., & Maguire, E. A. (2022). Interference suppression techniques for OPM-based MEG: Opportunities and challenges. *NeuroImage*, 247, 118834.

<https://doi.org/10.1016/j.neuroimage.2021.118834>

Singh S. P. (2014). Magnetoencephalography: Basic principles. *Annals of Indian Academy of Neurology*, 17(Suppl 1), S107–S112. <https://doi.org/10.4103/0972-2327.128676>

Stolk, A., Todorovic, A., Schoffelen, J. M., & Oostenveld, R. (2013). Online and offline tools for head movement compensation in MEG. *NeuroImage*, 68, 39–48.

<https://doi.org/10.1016/j.neuroimage.2012.11.047>

Stokkermans, M., Solis-Escalante, T., Cohen, M. X., & Weerdesteyn, V. (2023). Midfrontal theta dynamics index the monitoring of postural stability. *Cerebral Cortex*, 33(7), 3454–3466. <https://doi.org/10.1093/cercor/bhac283>

Tierney, T. M., Alexander, N., Mellor, S., Holmes, N., Seymour, R., O'Neill, G. C., Maguire, E. A., & Barnes, G. R. (2021). Modelling optically pumped magnetometer interference

in MEG as a spatially homogeneous magnetic field. *NeuroImage*, 244, 118484.

<https://doi.org/10.1016/j.neuroimage.2021.118484>

Tierney, T. M., Mellor, S., O'Neill, G. C., Timms, R. C., & Barnes, G. R. (2022). Spherical harmonic based noise rejection and neuronal sampling with multi-axis OPMs.

NeuroImage, 258, 119338. <https://doi.org/10.1016/j.neuroimage.2022.119338>

Tierney, T. M., Seedat, Z., Pier, K. St., Mellor, S., & Barnes, G. R. (2023). *Adaptive multipole models of OPM data* [Preprint]. Neuroscience.

<https://doi.org/10.1101/2023.09.11.557150>

Vrba, J., & Robinson, S. E. (2002). SQUID sensor array configurations for magnetoencephalography applications. *Superconductor Science and Technology*, 15(9), R51–R89. <https://doi.org/10.1088/0953-2048/15/9/201>

Zetter, R., Iivanainen, J., & Parkkonen, L. (2019). Optical Co-registration of MRI and On-scalp MEG. *Scientific Reports*, 9(1), 5490. <https://doi.org/10.1038/s41598-019-41763-4>